nature cell biology

Breast-cancer-secreted miR-122 reprograms glucose metabolism in premetastatic niche to promote metastasis

Miranda Y. Fong[1], Weiying Zhou[1], Liang Liu[1,2], Aileen Y. Alontaga[3], Manasa Chandra[1,4], Jonathan Ashby[5], Amy Chow[1], Sean Timothy Francis O'Connor[1], Shasha Li[1], Andrew R. Chin[1,4], George Somlo[6], Melanie Palomares[6,7], Zhuo Li[8], Jacob R. Tremblay[1,4], Akihiro Tsuyada[1], Guoqiang Sun[9], Michael A. Reid[1], Xiwei Wu[10], Piotr Swiderski[11], Xiubao Ren[2], Yanhong Shi[9], Mei Kong[1], Wenwan Zhong[5], Yuan Chen[3] and Shizhen Emily Wang[1,2,12]

Reprogrammed glucose metabolism as a result of increased glycolysis and glucose uptake is a hallmark of cancer. Here we show that cancer cells can suppress glucose uptake by non-tumour cells in the premetastatic niche, by secreting vesicles that carry high levels of the miR-122 microRNA. High miR-122 levels in the circulation have been associated with metastasis in breast cancer patients, and we show that cancer-cell-secreted miR-122 facilitates metastasis by increasing nutrient availability in the premetastatic niche. Mechanistically, cancer-cell-derived miR-122 suppresses glucose uptake by niche cells *in vitro* and *in vivo* by downregulating the glycolytic enzyme pyruvate kinase. *In vivo* inhibition of miR-122 restores glucose uptake in distant organs, including brain and lungs, and decreases the incidence of metastasis. These results demonstrate that, by modifying glucose utilization by recipient premetastatic niche cells, cancer-derived extracellular miR-122 is able to reprogram systemic energy metabolism to facilitate disease progression.

Reprogrammed energy metabolism to fuel rapid cell growth and proliferation is an emerging hallmark of cancer[1]. Most cancer cells use aerobic glycolysis with reduced mitochondrial oxidative phosphorylation for glucose metabolism even when oxygen is sufficient. This phenomenon, known as the 'Warburg effect', favours the uptake and incorporation of nutrients needed to produce a new cell[2]. To compensate for the consequent reduction in ATP production, cancer cells often adopt mechanisms to increase glucose uptake and utilization. One mechanism involves the regulation of glucose transporters, among which GLUT1 (also known as SLC2A1) is responsible for basal levels of glucose uptake in all cells[3]. GLUT1 can be regulated by the PI3K/AKT/mTOR pathway, which is frequently activated in cancer[4,5]. Furthermore, hypoxia can stimulate glucose uptake and metabolism through HIF-1 by inducing *GLUT3* and glycolytic genes *ALDA*, *PGK1* and *PKM* (pyruvate kinase; refs 6,7). It was recently reported that phosphorylation or sumoylation of PKM2 leads to translocation to the nucleus, where it acts as a transcriptional co-activator to induce *GLUT1*, *PDK1* and *HK1* (refs 8–13). Here we focus on a mechanism mediated by a cancer-secreted microRNA (miRNA) that reallocates glucose to favour uptake by cancer cells.

MiRNA negatively regulates gene expression by binding to the 3′ untranslated region (3′UTR) of messenger RNA, leading to degradation or translation blockade[14]. Deregulation of miRNA is tightly linked to cancer[15], and circulating miRNA has emerged as a potential biomarker for cancer diagnosis and prognosis[16–19]. MiRNA can be secreted into the extracellular environment through membrane-enclosed vesicles (such as exosomes) or in

[1]Department of Cancer Biology, City of Hope Beckman Research Institute, Duarte, California 91010, USA. [2]Department of Biotherapy and Key Laboratory of Cancer Immunology, Tianjin Medical University Cancer Institute and Hospital, Tianjin 300060, China. [3]Department of Molecular Medicine, City of Hope Beckman Research Institute, Duarte, California 91010, USA. [4]City of Hope Irell & Manella Graduate School of Biological Sciences, Duarte, California 91010, USA. [5]Department of Chemistry, University of California, Riverside, California 92521, USA. [6]Department of Medical Oncology, City of Hope Medical Center, Duarte, California 91010, USA. [7]Department of Population Sciences, City of Hope Beckman Research Institute, Duarte, California 91010, USA. [8]Core of Electron Microscopy, City of Hope Comprehensive Cancer Center, Duarte, California 91010, USA. [9]Department of Neurosciences, City of Hope Beckman Research Institute, Duarte, California 91010, USA. [10]Core of Integrative Genomics, City of Hope Comprehensive Cancer Center, Duarte, California 91010, USA. [11]Core of Synthetic and Biopolymer Chemistry, City of Hope Comprehensive Cancer Center, Duarte, California 91010, USA.
[12]Correspondence should be addressed to S.E.W. (e-mail: ewang@coh.org)

Received 28 April 2014; accepted 11 December 2014; published online 26 January 2015; DOI: 10.1038/ncb3094

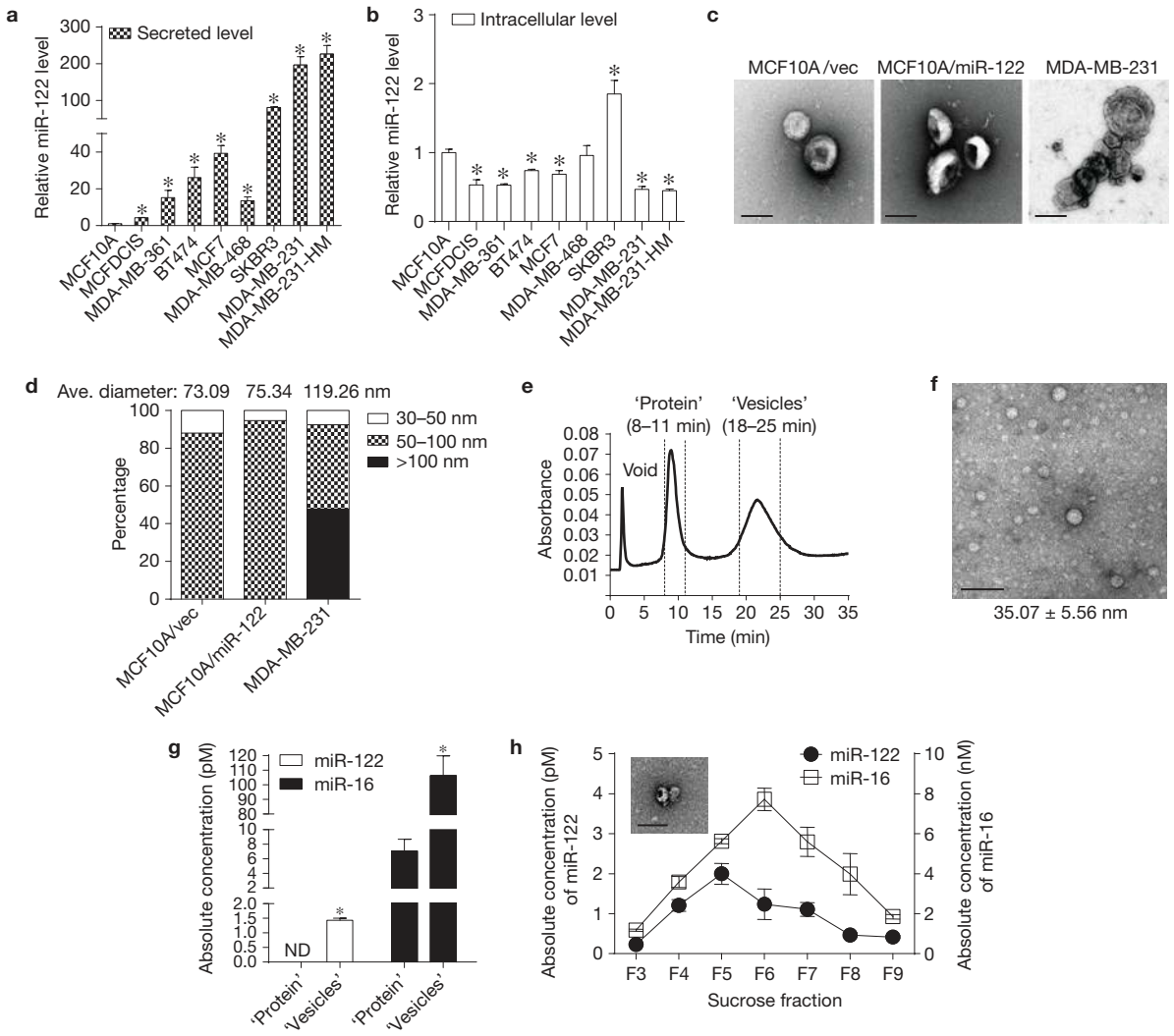

Figure 1 miR-122 is highly secreted by cancer cells. (**a**,**b**) RNA was extracted from the 110,000*g* medium pellet (**a**) and PBS-washed cells (**b**) and analysed for miR-122 by quantitative PCR with reverse transcription (RT-qPCR). Data were normalized to levels of total proteins (secreted; **a**) or U6 (cellular; **b**), and compared with the non-tumour line MCF10A ($n=6$ extracts). (**c**) Representative electron microscopy images of vesicles in the 110,000*g* medium pellet. Scale bar: 100 nm. (**d**) Size distribution of vesicles identified in the 110,000*g* medium pellets ($n=25$ vesicles for MCF10A/vec; $n=38$ for MCF10A/miR-122; $n=94$ for MDA-MB-231). (**e**) Fractogram (UV absorption at 280 nm) for the AF4 eluates characterizing the MDA-MB-231 110,000*g* medium pellet. (**f**) A representative electron microscopy image of MDA-MB-231-derived vesicles in the fraction eluted at 18–25 min. The measured diameter of vesicles is shown as mean ± s.d. ($n=41$). Scale bar: 100 nm. (**g**) RT-qPCR-determined levels of miR-122 and miR-16 in MDA-MB-231-derived protein and vesicle fractions separated by AF4 ($n=6$ extracts). Absolute miRNA levels are calculated on the basis of standard curves. ND: not detected. (**h**) After sucrose gradient centrifugation of MDA-MB-231-derived 110,000*g* medium pellet, the absolute miRNA level in each gradient fraction was determined by RT-qPCR and calculated on the basis of standard curves ($n=6$ extracts). A representative electron microscopy image of MDA-MB-231-derived vesicles in sucrose fraction 5 (F5) is shown. Scale bar: 100 nm. $^{*}P<0.05$ for all panels, derived from Kruskal–Wallis test. Data are represented as mean ± s.d. in all panels except **c**–**e**.

complexes with protein or lipid-based carriers[20,21]. Accumulating evidence demonstrates that miRNA as well as proteins can be transferred to neighbouring or distant cells in these secretory forms to modulate cell function[22–27]. Extracellular miRNA is therefore emerging as a new group of messengers and effectors in intercellular communication.

Several miRNAs have been implicated in metabolism and metabolic disorders[28]. Among them, miR-122 regulates cholesterol efflux, liver triglyceride content and the rate of β-oxidation[29]. Potential miR-122 targets have been analysed by luciferase-reporter-based 3′UTR screening, identifying *PKM* as one of the targets[30], which suggests that miR-122 may play a role in glucose metabolism. Our recent study in breast cancer (BC) patients identified higher levels of circulating miR-122 as a marker for predicting metastatic progression in early-stage BC (ref. 18). This urged us to investigate the function of extracellular miR-122 in cancer progression and metastasis. Here we demonstrate that cancer-secreted miR-122 can be transferred to normal cells in the premetastatic niches, thereby suppressing glucose utilization in these cells to accommodate the massive energy needs of cancer cells during metastatic growth.

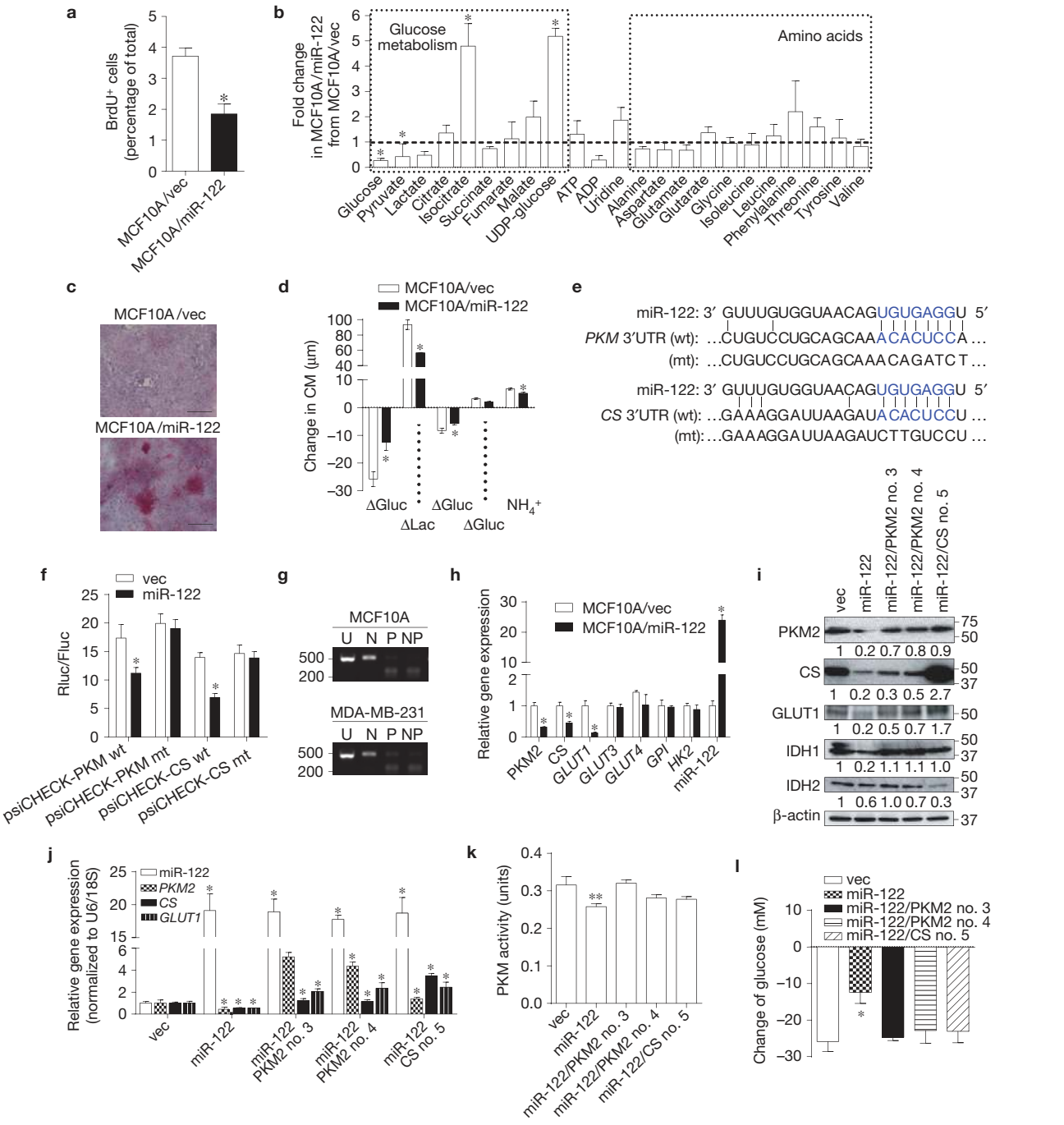

Figure 2 miR-122 suppresses glucose metabolism by downregulating PKM. (**a**) BrdU uptake in indicated cells was analysed by flow cytometry ($n=6$ biological replicates). (**b**) Quantification of intracellular metabolites by NMR spectroscopy ($n=3$ biological replicates). (**c**) Glycogen staining (red) in MCF10A/vec and MCF10A/miR-122 cells. Scale bar: 100 μm. (**d**) Change of metabolites in the CM after 72 h culture ($n=6$ biological replicates). (**e**) The predicted miR-122 binding site in the 3′UTR of the human *PKM* and *CS* genes. The corresponding sequence in the mutated (mt) version is also shown. (**f**) The psiCHECK reporters containing 3′UTR of human *PKM* and *CS* genes with wild-type (wt) or mutated (mt) miR-122 binding sites were used to transfect MCF10A cells stably expressing miR-122 or the empty vector (as control). Luciferase activity was analysed at 48 h post-transfection ($n=6$ extracts) and the ratio between *Renilla* luciferase and firefly luciferase activities (Rluc/Fluc) is shown. (**g**) Determination of PKM isoforms expressed in MCF10A and MDA-MB-231. RNA was subjected to RT-PCR followed by digestion with NcoI (N), PstI (P) or both enzymes (NP), plus an uncut control (U). Products were separated on an agarose gel with SYBR Safe. The presence of a PstI digestion site indicates the splicing isoform M2, whereas the NcoI site indicates isoform M1. Sizes of markers (in base pairs) are indicated. (**h**) RT-qPCR analysis showing the relative expression of indicated genes in MCF10A/miR-122 and MCF10A/vec cells ($n=6$ extracts). (**i**) Western blot analysis in MCF10A/miR-122 and MCF10A/vec cells with restored expression of PKM2 and CS. Sizes of markers (in kilodaltons, kDa) are indicated. (**j**) RT-qPCR analysis in selected colonies with restored expression of PKM2 and CS ($n=6$ extracts). (**k**) PKM activity (units) in 5 μg protein in indicated cells ($n=6$ extracts). (**l**) Change of glucose in the medium after 72 h culture of selected clones normalized to cell number ($n=3$ biological replicates). $^{*}P<0.05$, $^{**}P<0.01$ for all panels, derived from Kruskal–Wallis test. Data are represented as mean ± s.d. in all panels except **c**,**e**,**g** and **i**. Uncropped images of blots and gels are shown in Supplementary Fig. 5.

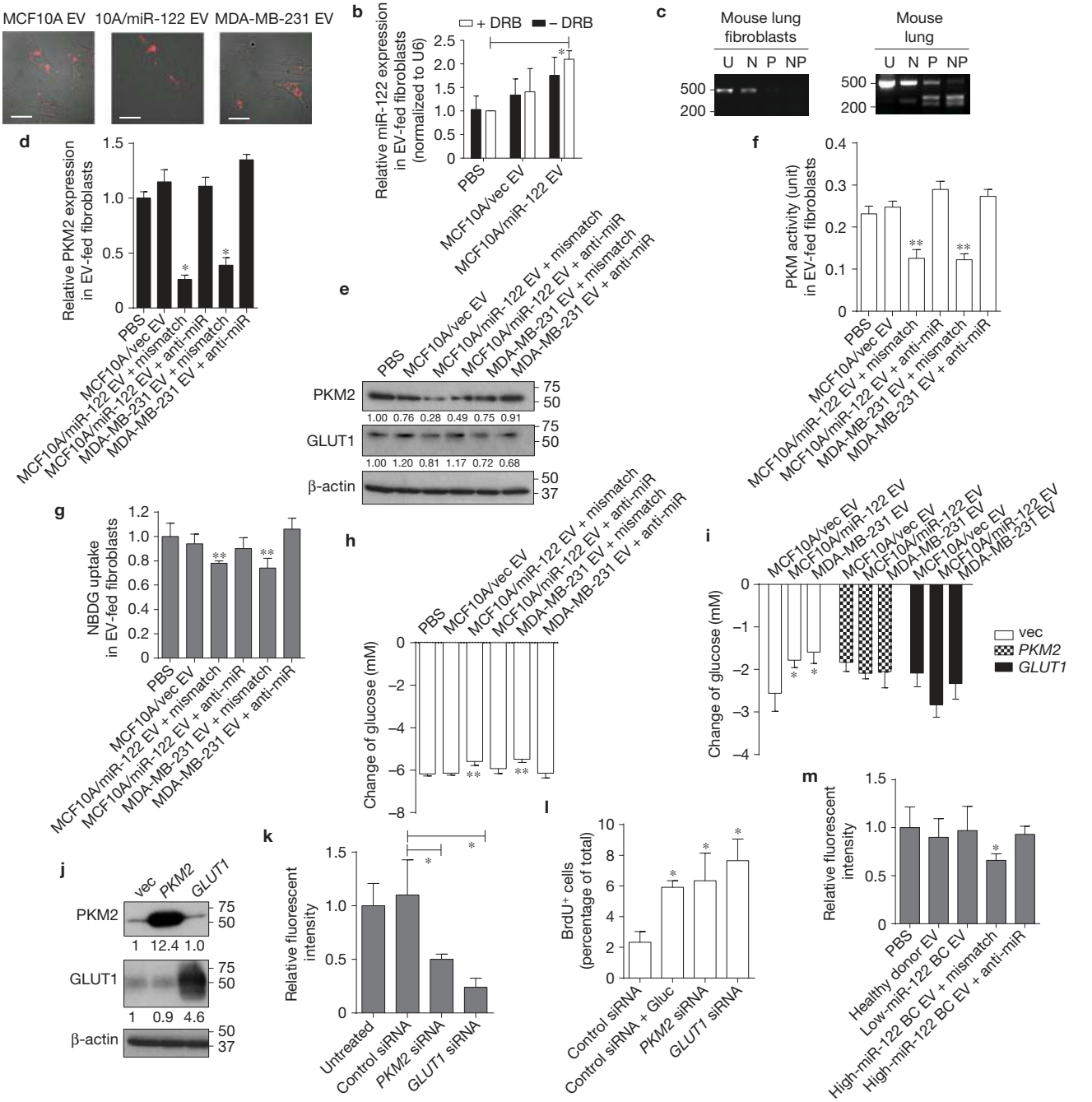

Figure 3 Cancer-secreted miR-122 downregulates glucose uptake in lung fibroblasts. (**a**) Uptake of 1,1′-dioctadecyl-3,3,3′3′-tetramethylindocarbo cyanine perchlorate (DiI)-labelled exosome-containing EVs (prepared from the 110,000*g* medium pellet) at 48 h. Scale bar: 60 μm. (**b**) Levels of miRNAs in fibroblasts pretreated with 10 μM RNA polymerase II inhibitor 5,6-dichloro-1-β-D-ribofuranoside (DRB) for 2 h followed by treatment with EVs for 16 h. miR-122 levels were normalized to U6 ($n=6$ extracts). (**c**) Determination of PKM isoforms in fibroblasts and mouse tissues by RT-PCR as indicated in Fig. 2g. Sizes of markers (in base pairs) are indicated. (**d**–**h**) Fibroblasts were treated with two doses of EVs from the indicated producer cells given 48 h apart and transfected with anti-miR-122 oligonucleotides or mismatch control oligonucleotides, before analysis at 96 h by (**d**) RT-qPCR ($n=6$ extracts), (**e**) western blot analysis (with marker size indicated in kDa), (**f**) PKM activity assay using 5 μg of proteins ($n=5$ biological replicates), (**g**) 2-NBDG uptake ($n=6$ biological replicates) and (**h**) change of glucose in the CM ($n=9$ biological replicates). (**i**) Change of glucose in the CM of fibroblasts transfected with expression plasmids containing the ORF but not 3′UTR of *PKM2* or *GLUT1*, or the empty vector, and treated with EVs from the indicated producer cells ($n=5$ biological replicates). (**j**) Western blot of fibroblasts transfected with expression plasmids for *PKM2* or *GLUT1*. Sizes of markers (in kDa) are indicated. (**k**) 2-NBDG uptake in siRNA-transfected fibroblasts ($n=5$ biological replicates). Fluorescent intensity was compared with the first column, which served as a control. (**l**) CM was collected from siRNA-transfected fibroblasts cultured for 72 h and the glucose concentration measured. The CM was then fed to MDA-MB-231-HM cells before proliferation was assessed by BrdU incorporation at 72 h ($n=6$ biological replicates). (**m**) Circulating EVs were extracted from pooled healthy donor sera and from BC patients' sera with low or high vesicular miR-122 and used to treat fibroblasts, and 2-NBDG uptake was measured ($n=8$ biological replicates). Fluorescent intensity was compared with the first column, which served as a control. $^{*}P<0.05$, $^{**}P<0.01$ for all panels, derived from Kruskal–Wallis test. Data are represented as mean ± s.d. in all panels except **a**,**c**,**e** and **j**. Uncropped images of blots and gels are shown in Supplementary Fig. 5.

RESULTS

miR-122 is highly secreted by cancer cells

We first examined the conditioned medium (CM) of various breast cell lines for miR-122 secretion. We focused on the 110,000*g* medium pellet that is known to contain extracellular vesicles (EVs) including exosomes and that carried the majority of extracellular miR-122, compared with the supernatant fraction (Supplementary Fig. 1a). All BC lines secreted significantly elevated miR-122 when compared with non-cancerous MCF10A (Fig. 1a). This was not accompanied by an elevated intracellular level, as most cancer lines exhibited reduced intracellular miR-122 (Fig. 1b). Whereas MCF10A-derived vesicles all exhibited a diameter of 30–100 nm, representing exosomes, vesicles from the BC line MDA-MB-231 were more heterogeneous and contained more than 50% exosomes, with the rest being microvesicles larger than 100 nm (Fig. 1c,d), consistent with a previous study[31]. Further characterization of the medium pellet by asymmetrical flow field flow fractionation (AF4; ref. 32) revealed two peaks representing proteins (eluted at 8–11 min) and vesicles (eluted at 18–25 min) measuring 30–60 nm (averaged $\approx$ 35 nm for MDA-MB-231), but a lack of high-density lipoproteins (eluted at 11–16 min; Fig. 1e,f and Supplementary Fig. 1b, ref. 32). For MDA-MB-231, miR-122 was exclusively detected in the vesicle but not the protein fraction, whereas forced overexpression of miR-122 in MCF10A increased miR-122 secretion predominantly in vesicles, with a slight induction also detected in protein-associated form (Fig. 1g and Supplementary Fig. 1c). Secretion of miR-122 by MCF10A cells engineered to stably overexpress the control vector (MCF10A/vec) was below the detection limit in fractionated samples. By gradient centrifugation of the medium pellet we further determined that, for both MDA-MB-231 and MCF10A-derived lines, miR-122 and miR-16 peaked in fractions 5 and 6, which contained vesicles measuring 30–100 nm (Fig. 1h and Supplementary Fig. 1d,e). Overall, our results indicate that cancer cells specifically secrete high levels of miR-122 into EVs including exosomes, and suggest that the potential effect of cancer-derived miR-122 may be ectopically observed in the recipient cells on EV-mediated transfer rather than in the cancer cells producing it.

miR-122 suppresses glucose metabolism by downregulating PKM

To study the function of miR-122, we first used MCF10A cells engineered to stably overexpress miR-122 (MCF10A/miR-122) or the control vector (MCF10A/vec). MCF10A/miR-122 had significantly reduced proliferation measured by 5-bromodeoxyuridine (BrdU) incorporation (Fig. 2a). Metabolome analysis of the cells revealed significantly decreased intracellular glucose and pyruvate in MCF10A/miR-122 (Fig. 2b and Supplementary Fig. 2), along with increased UDP-glucose (Fig. 2b) and glycogen staining (Fig. 2c) that is probably due to the excessive glucose spared from glycolysis going towards storage. In contrast, levels of amino acids were not significantly altered by miR-122. The ATP level in MCF10A/miR-122 was not significantly changed, which may reflect an adaptation of other metabolic pathways to meet the energy demand. Analyses of metabolites in the culture medium of MCF10A/miR-122 indicated about 50% decreased glucose uptake and about 40% reduced lactate production (Fig. 2d). Modestly diminished glutamine metabolism was also observed in these cells, possibly reflecting cell adaptation for the altered overall metabolic rate.

The metabolomic changes observed in MCF10A/miR-122 suggested a role for miR-122 in glucose metabolism. TargetScan and microRNA.org algorithms predicted a single, species-conserved miR-122 binding site in the 3′UTRs of pyruvate kinase (*PKM*) and citrate synthase (*CS*) genes (Fig. 2e). Therefore, we PCR-cloned the 3′UTRs and their seed-sequence-mutated versions downstream of the open reading frame (ORF) of a *Renilla* luciferase reporter gene and assessed the ability of miR-122 to downregulate luciferase expression. For both *PKM* and *CS*, the wild-type but not the mutated 3′UTR responded to miR-122 by directing about 50% reduction of reporter gene expression (Fig. 2f). Among a panel of genes controlling glucose metabolism, MCF10A/miR-122 exhibited significantly reduced PKM2 (isoform determined in Fig. 2g), CS and GLUT1 (Fig. 2h–j). Consistent with PKM2 downregulation, miR-122 also caused a significant reduction of PKM enzymatic activity (Fig. 2k).

To further determine if the miR-122-induced decrease in glucose consumption was mediated by PKM2 and/or CS downregulation, we restored the expression of these genes in MCF10A/miR-122 by overexpressing the *PKM2* or *CS* complementary DNA that lacked the 3′UTR. Both clones with fully or partially restored PKM activity (Fig. 2k) showed restored GLUT1 expression and glucose uptake from the medium that were comparable to those with MCF10A/vec (Fig. 2i,j,l). This is consistent with the previously reported ability of PKM2 to induce c-Myc and GLUT1 expression as a nuclear co-activator of β-catenin[9]. We noticed that restoration of CS by exogenous expression was always accompanied by elevated expression of endogenous PKM2 (Fig. 2i,j), possibly reflecting a natural feedback mechanism to accommodate the increased need for pyruvate by enhanced CS activity. Although this hindered us from dissecting the role of CS downregulation in mediating miR-122's function without the concomitant regulation of PKM2, our results indicate that restoration of PKM2 alone is sufficient to abolish the effect of miR-122 on glucose uptake; therefore, we chose to focus on this miR-122/PKM-mediated effect for the rest of this study.

Cancer-secreted miR-122 downregulates glucose consumption in niche cells

To study the ectopic effect of cancer-secreted miR-122, we focused on lung fibroblasts, brain astrocytes and neurons that are abundantly present in the premetastatic sites of BC. Primary lung fibroblasts exhibited efficient uptake of exosome-containing EVs regardless of the producer cells, as indicated by the internalization of DiI-labelled EVs (Fig. 3a). In these cells, EVs that are high in miR-122 caused significantly increased intracellular miR-122, which was not affected by an RNA polymerase II inhibitor (Fig. 3b), indicating that this increase of miR-122 reflects the EV-mediated miRNA transfer but not an induction of miR-122's endogenous expression. Also observed in high-miR-122 EV-treated fibroblasts were decreased expression of PKM2 and GLUT1 (Fig. 3c–e), along with decreased PKM activity (Fig. 3f). In addition, high-miR-122 EVs significantly reduced recipient cells' uptake of 2-[*N*-(7-nitrobenz-2-oxa-1,3-diazol-4-yl)amino]-2-deoxy-*D*-glucose (2-NBDG), a fluorescent analogue of glucose, which has been used to assess glucose transport in various cell types[33–36] (Fig. 3g), as well as their glucose consumption from the medium (Fig. 3h). These effects were significantly suppressed by treating recipient cells with anti-miR-122 (Fig. 3d–h).

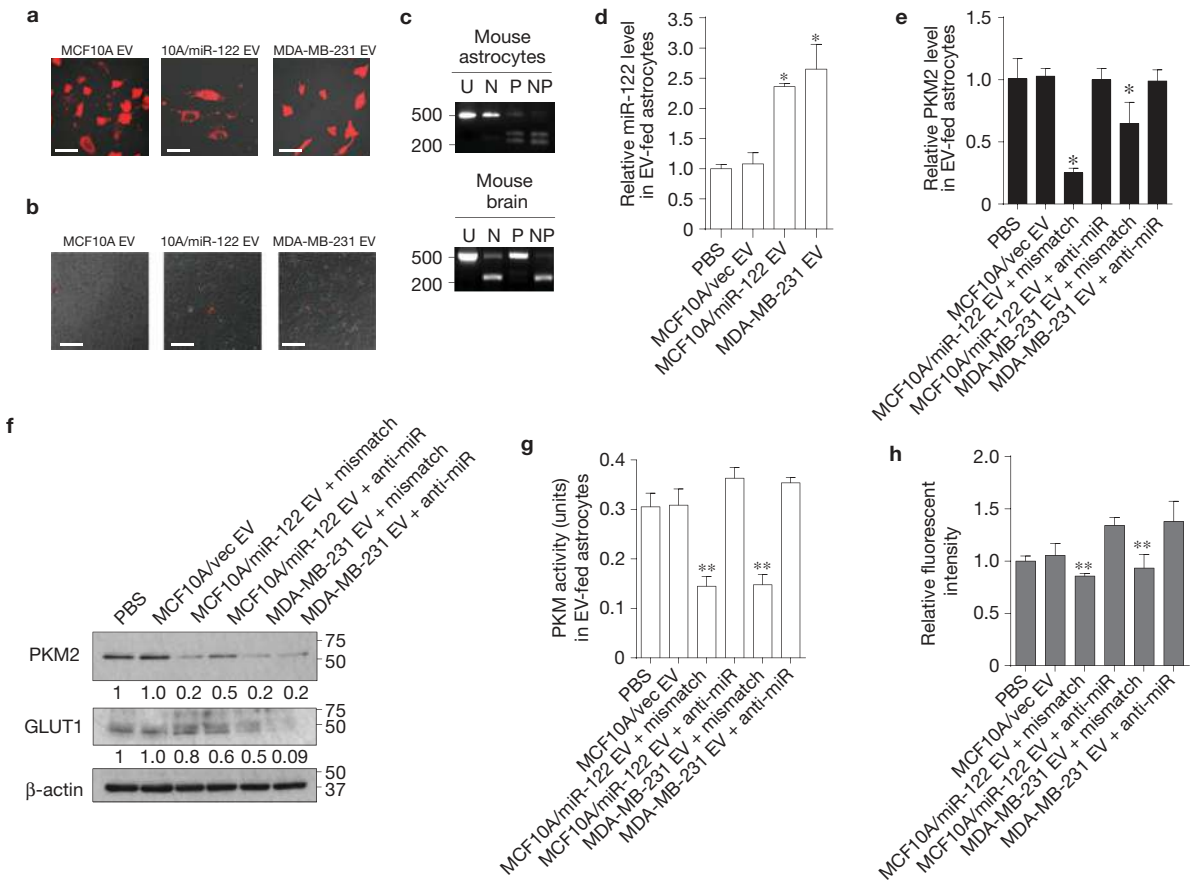

Figure 4 Cancer-secreted miR-122 downregulates glucose uptake in astrocytes. (**a**,**b**) EV uptake by astrocytes (**a**) and neurons (**b**). Indicated cells were incubated with DiI-labelled EVs (red) for 48 h before fluorescent and phase contrast microscopy images were captured. Scale bar: 60 μm. (**c**) Determination of PKM isoforms in primary mouse cells and mouse tissues by RT-PCR as indicated in Fig. 2g. Sizes of markers (in base pairs) are indicated. (**d**–**h**) Primary mouse astrocytes were treated with two doses of EVs from the indicated producer cells given 48 h apart, before being subjected to (**d**,**e**) RT-qPCR at 72 h for miR-122 ($n=6$ extracts) (**d**) and PKM2 ($n=6$ extracts) (**e**), (**f**) Western blot analysis for PKM2 and GLUT1 at 96 h (with marker size indicated in kDa), (**g**) PKM activity assay using 10 μg of proteins ($n=5$ biological replicates) and (**h**) 2-NBDG uptake assay ($n=5$ biological replicates). Fluorescent intensity was compared with the first column, which served as a control. $^{*}P<0.05$, $^{**}P<0.01$ for all panels, derived from Kruskal–Wallis test. Data are represented as mean ± s.d. in **d**,**e**,**g** and **h**. Uncropped images of blots and gels are shown in Supplementary Fig. 5.

Restored expression of PKM2 or GLUT1 by transfecting fibroblasts with the corresponding cDNA construct lacking 3′UTR abolished the effect of high-miR-122 EVs on fibroblast glucose consumption (Fig. 3i,j). In contrast, knockdown of either *PKM2* or *GLUT1* significantly reduced 2-NBDG uptake (Fig. 3k). We next assessed the effect of fibroblast glucose metabolism on proliferation of cancer cells sharing the same medium. Medium from fibroblasts treated with short interfering RNA (siRNA) against *PKM2* or *GLUT1* and therefore containing higher levels of residual glucose significantly enhanced proliferation of MDA-MB-231-HM cells, whereas medium collected from control fibroblasts needed to be supplemented with glucose to achieve this effect (Fig. 3l). We further examined the effect of circulating EVs isolated from the sera of healthy donors or BC patients. High-miR-122 EVs derived from a BC patient significantly reduced 2-NBDG uptake in fibroblasts when compared with healthy-donor- or patient-derived low-miR-122 EVs, and this effect was abolished by treating the fibroblasts with anti-miR-122 (Fig. 3m).

Glucose is the primary energy substrate in the mammalian brain, with astrocytes and neurons being the main consumers among other cell types[36–38]. Whereas primary astrocytes exhibited efficient uptake of EVs (Fig. 4a), neurons differentiated from embryonic neural stem cells exhibited poor EV uptake *in vitro* (Fig. 4b) and were therefore excluded from the current study. Similarly to lung fibroblasts, astrocytes treated with high-miR-122 EVs had significantly increased miR-122 in recipient cells, resulting in significantly decreased expression of PKM2 and GLUT1 (Fig. 4c–f), PKM activity (Fig. 4g) and 2-NBDG uptake (Fig. 4h) in an miR-122-dependent manner. Overall, these *in vitro* data indicate that vesicular transfer of miR-122 reduces glucose uptake by niche cells through downregulation of PKM2 and GLUT1, leading to enhanced cancer cell proliferation partially mediated by increased glucose availability to cancer cells.

Cancer-secreted miR-122 reprograms glucose consumption in niche tissues and promotes metastasis

To verify that cancer-secreted miR-122 modulates glucose metabolism in the premetastatic niches *in vivo*, we intravenously injected exosome-containing EVs with low or high levels of miR-122 into mice and measured glucose uptake in brain and lungs. Co-immunofluorescence

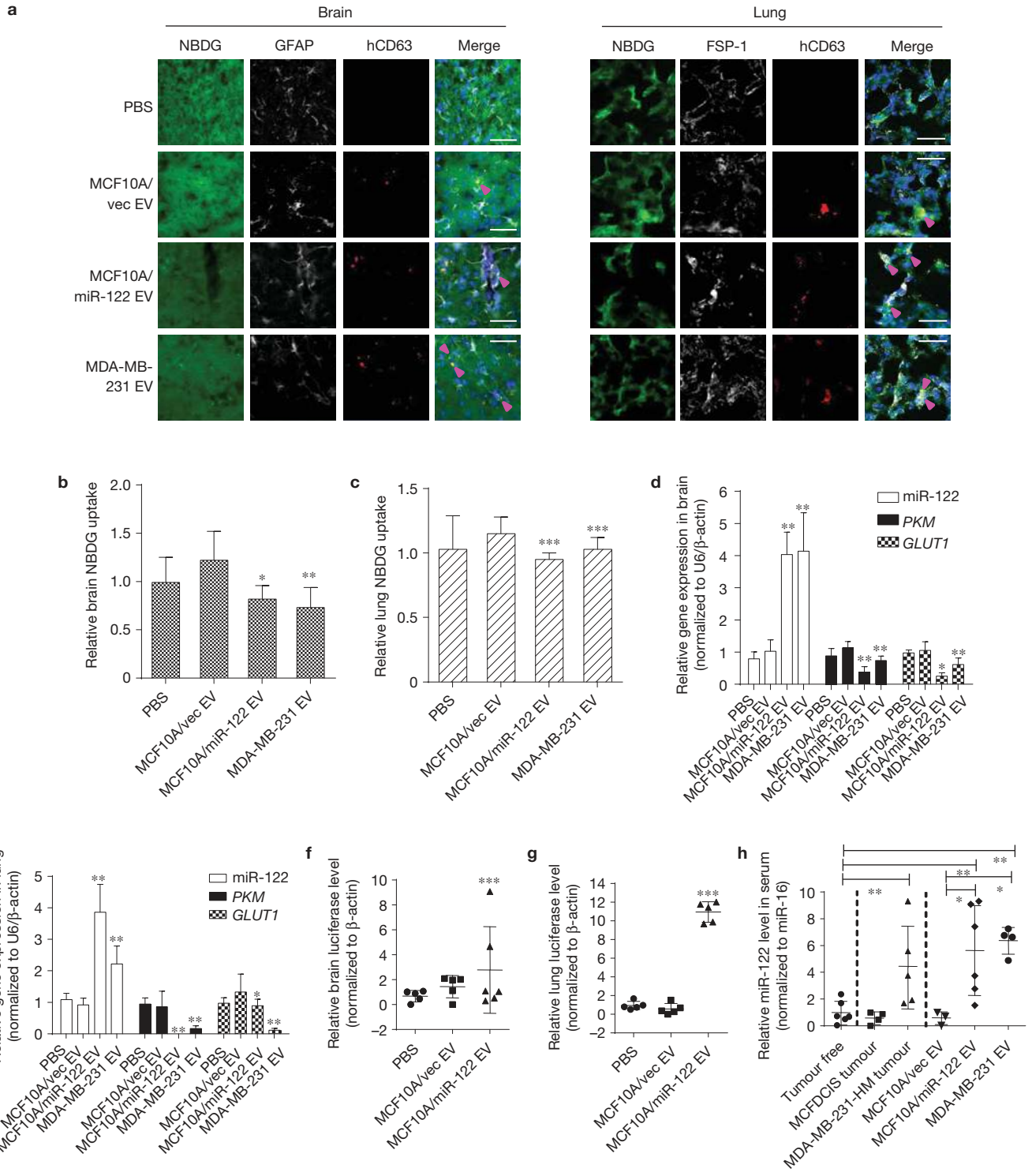

Figure 5 Vesicular transfer of miR-122 alters glucose uptake in niche tissues. Indicated EVs were intravenously injected into the tail veins of NOD/SCID/IL2Rγ-null (NSG) mice biweekly for 3.5 weeks. (**a**) Co-immunofluorescence of exosome marker CD63 (detected by a human-specific antibody; red) with astrocyte marker GFAP (white) or fibroblast marker FSP-1 (white) in brain and lung tissues of mice injected with 2-NBDG (green). Nuclei were counterstained with 4′,6-diamidino-2-phenylindole (DAPI) (blue). White bar: 20 μm. (**b**) Quantification of 2-NBDG uptake in brain ($n=20$ fields from four mice). (**c**) Quantification of 2-NBDG uptake in lung ($n=20$ fields from four mice). (**d**,**e**) RT-qPCR in brain (**d**) and lungs (**e**) ($n=9$ extracts from three mice). (**f**,**g**) Luciferase qPCR for the detection of metastases in the brain (**f**) and lungs (**g**) of mice pretreated with EVs followed by an intracardiac injection with luciferase-labelled MDA-MB-231-HM tumour cells ($n=15$ extracts from five mice). (**h**) miR-122 levels determined by RT-qPCR in the serum of non-tumour-bearing mice (group 1), mice bearing MCFDCIS or MDA-MB-231-HM tumours (groups 2 and 3) and non-tumour-bearing mice treated with EVs from MCF10A/vec, MCF10A/miR-122 or MDA-MB-231 cells (groups 4–6) ($n=15$ extracts from five mice). Data were normalized to the levels of miR-16. Data are represented as mean ± s.d. for all panels except **a**. $^{*}P<0.05$, $^{**}P<0.01$, $^{***}P<0.001$ for all panels, derived from Kruskal–Wallis test.

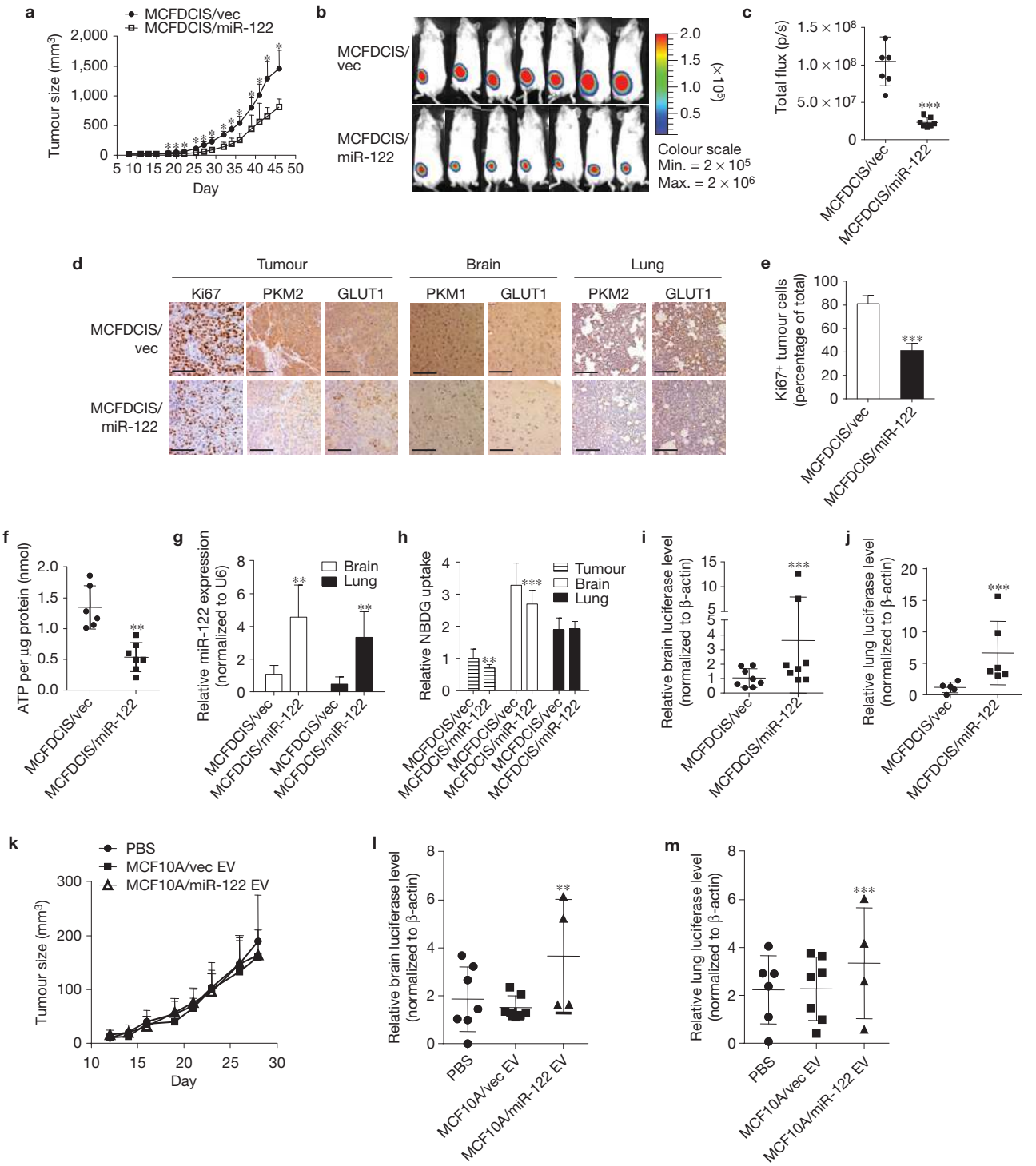

Figure 6 *In vivo* effect of miR-122 on primary tumour growth and metastasis. (**a**) Tumour growth curve in mice carrying MCFDCIS/vec and MCFDCIS/miR-122 orthotopic xenografts ($n=7$ mice). (**b**) Bioluminescence imaging (BLI) at week 3. (**c**) Luciferase quantification of **b** ($n=7$ mice). p/s: photons per second. (**d**) Immunohistochemistry (IHC) for Ki67, PKM1/2 and GLUT1 in tumour, brain and lung sections. Scale bar: 100 µm. (**e**) Quantification of Ki67⁺ tumour cells from three fields per tumour ($n=6$ mice per group). (**f**) Intratumoral levels of ATP assessed in tumour lysates by ENLIGHTEN ATP assay ($n=6$ mice per group). (**g**) miR-122 levels in the brain and lungs determined by RT-qPCR ($n=18$ extracts from six mice). (**h**) 2-NBDG uptake quantification in the tumour, brain and lungs ($n=12$ fields from four mice per group). (**i**,**j**) Luciferase qPCR in the brain (**i**, $n=24$ extracts from eight mice per group) and lungs (**j**, $n=18$ extracts from six mice per group) of MCFDCIS tumour-bearing mice. (**k**) Tumour growth curve in mice carrying orthotopic xenografts of MDA-MB-231 with stable knockdown of miR-122 (MDA-MB-231/122KD) and also receiving EV treatments as indicated ($n=7$ mice per group). No significant difference ($P>0.05$) between groups, on the basis of the Kruskal–Wallis test. (**l**,**m**) Luciferase qPCR for detection of metastases in the brain (**l**) and lungs (**m**) of mice bearing MDA-MB-231/122KD tumours and treated with the indicated EVs ($n=12$ extracts from four mice per group). $^{*}P<0.05$, $^{**}P<0.01$, $^{***}P<0.001$ for all panels, derived from Kruskal–Wallis test. Data are represented as mean ± s.d. in all panels except **b** and **d**.

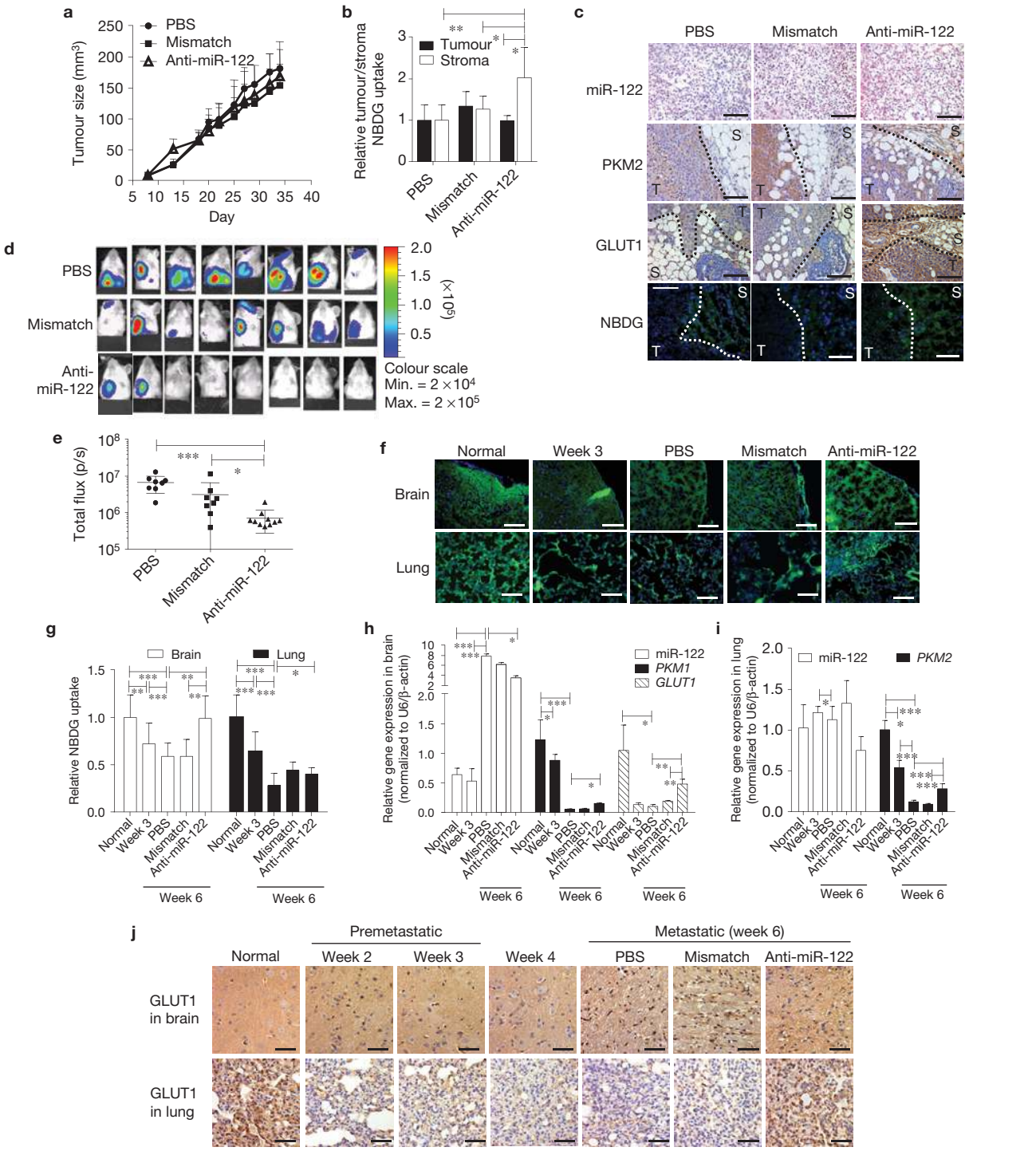

Figure 7 miR-122 intervention alleviates cancer-induced glucose reallocation *in vivo* and reduces metastasis. Luciferase-labelled MDA-MB-231-HM cells were injected into the no 4 mammary fat pad of NSG mice. Mice were divided into three groups ($n=8$ mice per group) for treatment with PBS, anti-miR-122 or mismatch control oligonucleotides. (**a**) Tumour growth curve ($n=8$ mice). No significant difference ($P>0.05$) between groups, on the basis of the Kruskal–Wallis test. (**b**) 2-NBDG uptake in the tumour and tumour-adjacent stroma ($n=20$ fields from four mice per group). (**c**) Primary tumour sections were analysed by IHC (for PKM2 and GLUT1) and *in situ* hybridization (ISH) (for miR-122). For 2-NBDG (green) uptake, sections were counterstained with DAPI (blue) to show nuclei. The dotted lines delineate tumour (T) from stroma (S). White bar: 100 μm. (**d**) BLI at week 5 indicating extensive brain and lung metastases in PBS and mismatch groups and reduced incidence of metastasis in anti-miR-122 group. (**e**) Quantification of BLI at week 5 ($n=8$ mice per group). p/s: photons per second. (**f**) Representative images of 2-NBDG uptake fluorescence. White bar: 60 μm. (**g**) Quantification of 2-NBDG uptake in the brain and lungs of tumour-free (normal) NSG mice and tumour-bearing mice that were untreated when killed at week 3 after tumour cell implantation or treated as indicated and killed at week 6 ($n=20$ fields from four mice per group). (**h**,**i**) RT-qPCR in brain (**h**) and lungs (**i**) of tumour-free and tumour-bearing mice ($n=12$ extracts from four mice per group). (**j**) GLUT1 IHC in brain and lungs. Scale bar: 60 μm. Data are represented as mean ± s.d. in all panels except **c**,**d**,**f** and **j**. $^{*}P<0.05$, $^{**}P<0.01$, $^{***}P<0.001$ for all panels, derived from Kruskal–Wallis test.

of cell-type-specific markers for astrocytes and fibroblasts and a human-specific exosomal marker, CD63, demonstrated that human-derived EVs can be received by these niche cell types *in vivo* (Fig. 5a). Both brain and lungs showed reduced 2-NBDG uptake as a consequence of receiving vesicular miR-122, which resulted in reduced expression of PKM and GLUT1 (Fig. 5b–e).

In another experiment, mice were pretreated with EVs before an intracardiac injection of luciferase-labelled MDA-MB-231-HM cells. Three weeks later, metastases in the brain and lungs were quantified by luciferase qPCR and confirmed by histology. Among mice receiving high-miR-122 EVs, all exhibited significant metastatic colonization in lungs and brain, whereas no metastases were observed in mice treated with MCF10A/vec EVs or PBS (Fig. 5f,g). Serum miR-122 levels were comparable between mice receiving high-miR-122 EVs and those bearing MDA-MB-231-HM tumours that naturally secrete miR-122 (Fig. 5h). Therefore, vesicular miR-122 results in reprogramming of niche tissue glucose utilization as a possible mechanism to promote circulating tumour cell colonization.

miR-122 overexpression reduces primary tumour growth while enhancing metastasis

To determine if the miR-122 level in primary tumours regulates tumour growth and if the primary-tumour-secreted miR-122 adapts the premetastatic niches to promote metastasis, we stably overexpressed miR-122 in an MCF10A-derived tumorigenic line, MCFDCIS, which forms comedo ductal carcinoma *in situ*-like lesions that spontaneously progress to invasive tumours[39]. miR-122 overexpression reduced cell proliferation, glucose uptake and the expression of PKM2, CS and GLUT1 *in vitro* (Supplementary Fig. 3a–d). Orthotopic xenograft tumours of MCFDCIS/miR-122 were significantly smaller than MCFDCIS/vec tumours (Fig. 6a–c), containing decreased numbers of $Ki67^{+}$ tumour cells, reduced expression of PKM2 and GLUT1 and decreased ATP level (Fig. 6d–f).

Mice bearing MCFDCIS/miR-122 tumours had increased miR-122 and decreased PKM1/2 and GLUT1 in the brain and lungs as well as significantly reduced 2-NBDG uptake in the brain, which was not observed in the lungs at the time of tissue collection (Fig. 6d,g,h). These mice also had significantly enhanced metastases to the brain and lungs (Fig. 6i,j), suggesting that miR-122 reduces primary tumour cell proliferation by restricting glucose uptake while simultaneously reprogramming the premetastatic niches to promote tumour cell colonization and metastatic formation.

To further focus on the niche-adapting effect of extracellular miR-122 by blocking its function inside cancer cells, we generated luciferase-labelled MDA-MB-231 cells stably expressing an anti-miR-122, which exhibited significantly reduced intracellular and secreted miR-122 and increased PKM2 (Supplementary Fig. 3e). Orthotopic xenograft tumours of these cells were established in mice that also received EV treatments. Although no difference in primary tumour growth was observed among all groups, mice receiving high-miR-122 EVs developed more metastases in brain and lungs (Fig. 6k–m).

Systemic miR-122 intervention alleviates cancer-induced glucose reallocation *in vivo* and reduces metastasis

To study the *in vivo* effect of systemic miR-122 intervention, xenograft tumours of MDA-MB-231-HM that naturally secreted high-miR-122 EVs were established, and mice were randomized into three treatment groups, which received PBS, mismatch control oligonucleotides or anti-miR-122 oligonucleotides. Although there was no difference in primary tumour size among the three groups (Fig. 7a and Supplementary Fig. 4), increased 2-NBDG uptake and enhanced staining of PKM2 and GLUT1 were observed in tumour-adjacent stromal cells in anti-miR-122-treated mice (Fig. 7b,c).

At week 5 we started to observe a lower incidence of metastasis to the brain and lungs in mice receiving anti-miR-122 treatment (Fig. 7d,e). At the premetastatic stage, when there were no detectable metastases by luciferase PCR, both organs showed reduced 2-NBDG uptake when compared with non-tumour-bearing mice (Fig. 7f,g), suggesting that factors secreted by the primary tumour can regulate glucose utilization in a distant organ in preparation for metastasis. This effect became more pronounced as cancer progressed, as a further reduction in 2-NBDG uptake was observed in the metastasis-free areas of brain and lungs at week 6 when metastases had developed in these organs (Fig. 7f,g; PBS group). Notably, treatment with anti-miR-122 but not the mismatch control oligonucleotides significantly alleviated tumour-derived suppression of glucose uptake in the brain, although the restoration was not significant in the lungs (Fig. 7f,g). In the brain, miR-122 levels increased with tumour progression, with a significant reduction in mice receiving anti-miR-122 oligonucleotides. Supporting our *in vitro* data, we noticed a concomitant decrease in the levels of PKM1 (isoform determined in Fig. 4c) and GLUT1 during tumour progression, which was alleviated by anti-miR-122 treatment (Fig. 7h,j). In the lung, anti-miR-122 oligonucleotides alleviated cancer-induced suppression of PKM2 and GLUT1 (Fig. 7i,j). Taken together, our *in vitro* and *in vivo* data indicate that cancer cells can induce glucose reallocation in the premetastatic microenvironments by suppressing glucose utilization in niche cells and enabling more glucose to be available to cancer cells, thereby facilitating metastatic cancer growth. This effect is at least partially mediated by cancer-secreted miR-122.

DISCUSSION

Our study demonstrates that miR-122 is highly secreted by BC cells and can promote metastasis by adapting the metabolic environment in a premetastatic niche, providing an understanding of our previous observation that miR-122 levels in the circulation are associated with metastatic progression in BC patients[18]. In addition to EVs, other protein and lipoprotein carriers of circulating miRNAs have been identified[40,41]. Although we cannot exclude the potential role for these other forms of extracellular miR-122 from our mechanism identified herein, characterization of the 110,000*g* medium pellet used in our study by AF4 and gradient centrifugation indicates that EVs of 30–100 nm are a major component of this material and capable of transferring miR-122 from cancer to normal niche cells to promote metastasis. An interesting phenomenon of stromal–epithelial metabolic coupling, termed the reverse Warburg effect for stromal glycolysis and cancer cell oxidative phosphorylation, has been recently recognized[42]. In BC, cancer-associated stromal cells rely on glycolysis to provide energy metabolites to cancer cells through monocarboxylate transporters during disease progression[43]. Endothelial cells also rely on glycolytic metabolism to support vessel sprouting for angiogenesis[43]. Although extracellular miR-122 does not

seem to contribute to increased glycolysis in cells in the primary tumour microenvironment, on the basis of the concomitant decrease in lactate production on miR-122-mediated reduction of glucose uptake (Fig. 2d and Supplementary Fig. 3b) and lack of change in most tricarboxylic acid cycle metabolites (Fig. 2b), other miRNAs in cancer-secreted EVs may contribute to this effect, which would be an interesting future direction. In exploring what caused the increase of isocitrate in MCF10A/miR-122 (Fig. 2b), we found that isocitrate dehydrogenase (IDH) 1 and 2 were both downregulated by miR-122 (Fig. 2i). Although a search of the 3′UTR of IDH1/2 did not reveal any miR-122 binding site, restoration of PKM2 was able to restore IDH1/2 levels in MCF10A/miR-122, suggesting that, similarly to GLUT1, IDH1/2 might be directly or indirectly regulated by PKM2. We also examined the NMR spectrum for α-ketoglutarate, which could not be reliably quantified owing to the low concentrations. However, the spectrum did suggest a reduction of α-ketoglutarate in MCF10A/miR-122 (Supplementary Fig. 2e), which is consistent with decreased IDH1/2 and increased isocitrate in these cells.

Adaptation of a premetastatic niche, initially defined by Kaplan and Lyden *et al.*[44,45], before the arrival of tumour cells, has been recognized as an important means for cancers to facilitate their sustained growth and metastasis[46,47]. Exosomes from highly metastatic melanomas 'educate' bone marrow progenitor cells towards a prometastatic phenotype and induce vascular leakiness at premetastatic sites to facilitate metastasis[26]. Melanoma-derived exosomes also prepare sentinel lymph nodes for metastasis by inducing cell recruitment, extracellular matrix remodelling and vascular growth factors[48]. In renal cell carcinoma, microvesicles derived from $CD105^+$ tumour-initiating cells trigger angiogenesis, which serves to enhance lung metastasis[49]. Further studies have highlighted the importance of other tumour-secreted factors resulting in establishment of a premetastatic niche[50–54].

Here we added a unique aspect of nutrient utilization to this paradigm of cancer–host crosstalk. Enhanced glucose uptake is common in cancer as a result of the high energy demand in cancer cells and the low ATP-generating efficiency due to the Warburg effect. GLUT1 and glycolytic enzymes have been shown to be upregulated in BC (refs 55,56) as potential mechanisms for increasing glucose uptake. Cancer cells also develop strategies to increase their availability to glucose, such as angiogenesis to gain nutrients from the blood. Here we provide evidence that cancer cells also systemically suppress the nutrient utilization by other cell types to favour themselves. This miR-122-mediated mechanism may be more important at an early stage before cancer-induced angiogenesis, when the availability of nutrients in the tumour microenvironment becomes limited to sustain tumour growth, and when disseminated tumour cells arrive at a distant tissue to prepare for rapid expansion among the surrounding normal niche cells, which are native competitors for nutrients. Indeed, we observed that BC cells at the primary site were able to affect glucose uptake by brain and lungs at a premetastatic stage (Fig. 7f–j). Importantly, miR-122 intervention using antisense oligonucleotides significantly reduced BC metastasis to brain and lungs (Fig. 7d,e). Thus, our previous[18] and current studies indicate that cancer-derived circulating miR-122 has the potential to be both a predictive marker and a therapeutic target for metastatic BC. As miR-122 antagonists are in clinical trials for patients with hepatitis C infection and exhibit good tolerance with a low propensity for drug interactions[57,58], miR-122-targeted therapy in cancer patients seems highly feasible, and the non-invasive blood test for circulating miR-122 would enable accurate selection of patients who may benefit from this treatment. □

METHODS

Methods and any associated references are available in the online version of the paper.

Note: Supplementary Information is available in the online version of the paper

ACKNOWLEDGEMENTS

This work was supported by the United States Army Research and Material Command grant W81-14-1-0029 (M.Y.F.), National Institutes of Health (NIH)/National Cancer Institute (NCI) grants R01CA166020 (S.E.W.) and R01CA163586 (S.E.W.), California Breast Cancer Research Program grant 20IB-0118 (S.E.W.), Breast Cancer Research Foundation-AACR grant 12-60-26-WANG (S.E.W.) and the City of Hope Women's Cancer Program. Research reported here includes work carried out in Core Facilities supported by the NIH/NCI under grant number P30CA33572. We thank A. Riggs, E. Roberts, L. Malkas, S. Kane, S. Chen, J. Mortimer and P. Sarnow for valuable comments, as well as the Core Facilities at City of Hope for services.

AUTHOR CONTRIBUTIONS

S.E.W. conceived ideas, and M.Y.F., Y.C. and X.R. contributed to project planning. M.Y.F. and S.E.W. designed and carried out the experiments. W.Zhou, L.L., A.C., S.T.F.O., S.L., A.R.C. and J.R.T. assisted with EV preparation and mouse experiments. G.Somlo and M.P. assisted with patient serum samples. Z.L. assisted with electron microscopy. A.T. assisted with mouse lung fibroblast culture. A.Y.A., M.C. and Y.C. assisted with NMR analysis. J.A. and W.Zhong assisted with AF4 analysis. G.Sun and Y.S. assisted with neuron culture. M.A.R. and M.K. assisted with medium metabolite analysis. X.W. assisted with bioinformatics analysis of miR-122 targets. P.S. assisted with anti-miR-122 and mismatch oligonucleotide synthesis. S.E.W. and M.Y.F. wrote the manuscript.

COMPETING FINANCIAL INTERESTS

The authors declare no competing financial interests.

Published online at www.nature.com/doifinder/10.1038/ncb3094
Reprints and permissions information is available online at www.nature.com/reprints

1. Hanahan, D. & Weinberg, R. A. Hallmarks of cancer: the next generation. *Cell* **144,** 646–674 (2011).
2. Vander Heiden, M. G., Cantley, L. C. & Thompson, C. B. Understanding the Warburg effect: the metabolic requirements of cell proliferation. *Science* **324,** 1029–1033 (2009).
3. Zhao, F. Q. & Keating, A. F. Functional properties and genomics of glucose transporters. *Curr. Genomics* **8,** 113–128 (2007).
4. DeBerardinis, R. J., Lum, J. J., Hatzivassiliou, G. & Thompson, C. B. The biology of cancer: metabolic reprogramming fuels cell growth and proliferation. *Cell Metab.* **7,** 11–20 (2008).
5. Barthel, A. *et al.* Regulation of GLUT1 gene transcription by the serine/threonine kinase Akt1. *J. Biol. Chem.* **274,** 20281–20286 (1999).
6. O'Rourke, J. F., Pugh, C. W., Bartlett, S. M. & Ratcliffe, P. J. Identification of hypoxically inducible mRNAs in HeLa cells using differential-display PCR. Role of hypoxia-inducible factor-1. *Eur. J. Biochem.* **241,** 403–410 (1996).
7. Semenza, G. L., Roth, P. H., Fang, H. M. & Wang, G. L. Transcriptional regulation of genes encoding glycolytic enzymes by hypoxia-inducible factor 1. *J. Biol. Chem.* **269,** 23757–23763 (1994).
8. Spoden, G. A. *et al.* The SUMO-E3 ligase PIAS3 targets pyruvate kinase M2. *J. Cell Biochem.* **107,** 293–302 (2009).
9. Yang, W. *et al.* ERK1/2-dependent phosphorylation and nuclear translocation of PKM2 promotes the Warburg effect. *Nat. Cell Biol.* **14,** 1295–1304 (2012).
10. Gao, X., Wang, H., Yang, J. J., Liu, X. & Liu, Z. R. Pyruvate kinase M2 regulates gene transcription by acting as a protein kinase. *Mol. Cell* **45,** 598–609 (2012).
11. Yang, W. *et al.* Nuclear PKM2 regulates β-catenin transactivation upon EGFR activation. *Nature* **480,** 118–122 (2011).
12. Lee, J., Kim, H. K., Han, Y. M. & Kim, J. Pyruvate kinase isozyme type M2 (PKM2) interacts and cooperates with Oct-4 in regulating transcription. *Int. J. Biochem. Cell Biol.* **40,** 1043–1054 (2008).
13. Luo, W. *et al.* Pyruvate kinase M2 is a PHD3-stimulated coactivator for hypoxia-inducible factor 1. *Cell* **145,** 732–744 (2011).
14. Bartel, D. P. MicroRNAs: target recognition and regulatory functions. *Cell* **136,** 215–233 (2009).

15. Calin, G. A. & Croce, C. M. MicroRNA signatures in human cancers. *Nat. Rev. Cancer* **6,** 857–866 (2006).
16. Mitchell, P. S. *et al.* Circulating microRNAs as stable blood-based markers for cancer detection. *Proc. Natl Acad. Sci. USA* **105,** 10513–10518 (2008).
17. Taylor, D. D. & Gercel-Taylor, C. MicroRNA signatures of tumor-derived exosomes as diagnostic biomarkers of ovarian cancer. *Gynecol. Oncol.* **110,** 13–21 (2008).
18. Wu, X. *et al.* De novo sequencing of circulating miRNAs identifies novel markers predicting clinical outcome of locally advanced breast cancer. *J. Transl. Med.* **10,** 42 (2012).
19. Zhu, W., Qin, W., Atasoy, U. & Sauter, E. R. Circulating microRNAs in breast cancer and healthy subjects. *BMC Res. Notes* **2,** 89 (2009).
20. Zen, K. & Zhang, C. Y. Circulating microRNAs: a novel class of biomarkers to diagnose and monitor human cancers. *Med. Res. Rev.* **32,** 326–348 (2012).
21. Redis, R. S., Calin, S., Yang, Y., You, M. J. & Calin, G. A. Cell-to-cell miRNA transfer: from body homeostasis to therapy. *Pharmacol. Ther.* **136,** 169–174 (2012).
22. Valadi, H. *et al.* Exosome-mediated transfer of mRNAs and microRNAs is a novel mechanism of genetic exchange between cells. *Nat. Cell Biol.* **9,** 654–659 (2007).
23. Wang, K., Zhang, S., Weber, J., Baxter, D. & Galas, D. J. Export of microRNAs and microRNA-protective protein by mammalian cells. *Nucleic Acids Res.* **38,** 7248–7259 (2010).
24. Vickers, K. C. & Remaley, A. T. Lipid-based carriers of microRNAs and intercellular communication. *Curr. Opin. Lipidol.* **23,** 91–97 (2012).
25. Skog, J. *et al.* Glioblastoma microvesicles transport RNA and proteins that promote tumour growth and provide diagnostic biomarkers. *Nat. Cell Biol.* **10,** 1470–1476 (2008).
26. Peinado, H. *et al.* Melanoma exosomes educate bone marrow progenitor cells toward a pro-metastatic phenotype through MET. *Nat. Med.* **18,** 883–891 (2012).
27. Zhou, W. *et al.* Cancer-secreted miR-105 destroys vascular endothelial barriers to promote metastasis. *Cancer Cell* **25,** 501–515 (2014).
28. Rottiers, V. & Naar, A. M. MicroRNAs in metabolism and metabolic disorders. *Nat. Rev. Mol. Cell Biol.* **13,** 239–250 (2012).
29. Moore, K. J., Rayner, K. J., Suarez, Y. & Fernandez-Hernando, C. The role of microRNAs in cholesterol efflux and hepatic lipid metabolism. *Annu. Rev. Nutr.* **31,** 49–63 (2011).
30. Boutz, D. R. *et al.* Two-tiered approach identifies a network of cancer and liver disease-related genes regulated by miR-122. *J. Biol. Chem.* **286,** 18066–18078 (2011).
31. Palma, J. *et al.* MicroRNAs are exported from malignant cells in customized particles. *Nucleic Acids Res.* **40,** 9125–9138 (2012).
32. Ashby, J. *et al.* Distribution profiling of circulating MicroRNAs in serum. *Anal. Chem.* **86,** 9343–9349 (2014).
33. Lloyd, P. G., Hardin, C. D. & Sturek, M. Examining glucose transport in single vascular smooth muscle cells with a fluorescent glucose analog. *Physiol. Res.* **48,** 401–410 (1999).
34. Loaiza, A., Porras, O. H. & Barros, L. F. Glutamate triggers rapid glucose transport stimulation in astrocytes as evidenced by real-time confocal microscopy. *J. Neurosci.* **23,** 7337–7342 (2003).
35. Yamada, K. *et al.* Measurement of glucose uptake and intracellular calcium concentration in single, living pancreatic β-cells. *J. Biol. Chem.* **275,** 22278–22283 (2000).
36. Itoh, Y., Abe, T., Takaoka, R. & Tanahashi, N. Fluorometric determination of glucose utilization in neurons *in vitro* and *in vivo*. *J. Cereb. Blood Flow Metab.* **24,** 993–1003 (2004).
37. Chuquet, J., Quilichini, P., Nimchinsky, E. A. & Buzsaki, G. Predominant enhancement of glucose uptake in astrocytes versus neurons during activation of the somatosensory cortex. *J. Neurosci.* **30,** 15298–15303 (2010).
38. Bak, L. K., Schousboe, A., Sonnewald, U. & Waagepetersen, H. S. Glucose is necessary to maintain neurotransmitter homeostasis during synaptic activity in cultured glutamatergic neurons. *J. Cereb. Blood Flow Metab.* **26,** 1285–1297 (2006).
39. Hu, M. *et al.* Regulation of *in situ* to invasive breast carcinoma transition. *Cancer Cell* **13,** 394–406 (2008).
40. Vickers, K. C., Palmisano, B. T., Shoucri, B. M., Shamburek, R. D. & Remaley, A. T. MicroRNAs are transported in plasma and delivered to recipient cells by high-density lipoproteins. *Nat. Cell Biol.* **13,** 423–433 (2011).
41. Arroyo, J. D. *et al.* Argonaute2 complexes carry a population of circulating microRNAs independent of vesicles in human plasma. *Proc. Natl Acad. Sci. USA* **108,** 5003–5008 (2011).
42. Pavlides, S. *et al.* The reverse Warburg effect: aerobic glycolysis in cancer associated fibroblasts and the tumor stroma. *Cell Cycle* **8,** 3984–4001 (2009).
43. Martinez-Outschoorn, U. E., Lisanti, M. P. & Sotgia, F. Catabolic cancer-associated fibroblasts transfer energy and biomass to anabolic cancer cells, fueling tumor growth. *Semin. Cancer Biol.* **25,** 47–60 (2014).
44. Kaplan, R. N., Psaila, B. & Lyden, D. Bone marrow cells in the 'pre-metastatic niche': within bone and beyond. *Cancer Metastasis Rev.* **25,** 521–529 (2006).
45. Kaplan, R. N. *et al.* VEGFR1-positive haematopoietic bone marrow progenitors initiate the pre-metastatic niche. *Nature* **438,** 820–827 (2005).
46. Peinado, H., Lavotshkin, S. & Lyden, D. The secreted factors responsible for pre-metastatic niche formation: old sayings and new thoughts. *Semin. Cancer Biol.* **21,** 139–146 (2011).
47. Sethi, N. & Kang, Y. Unravelling the complexity of metastasis - molecular understanding and targeted therapies. *Nat. Rev. Cancer* **11,** 735–748 (2011).
48. Hood, J. L., San, R. S. & Wickline, S. A. Exosomes released by melanoma cells prepare sentinel lymph nodes for tumor metastasis. *Cancer Res.* **71,** 3792–3801 (2011).
49. Grange, C. *et al.* Microvesicles released from human renal cancer stem cells stimulate angiogenesis and formation of lung premetastatic niche. *Cancer Res.* **71,** 5346–5356 (2011).
50. Erler, J. T. *et al.* Hypoxia-induced lysyl oxidase is a critical mediator of bone marrow cell recruitment to form the premetastatic niche. *Cancer Cell* **15,** 35–44 (2009).
51. Hiratsuka, S. *et al.* Primary tumours modulate innate immune signalling to create pre-metastatic vascular hyperpermeability foci. *Nat. Commun.* **4,** 1853 (2013).
52. Hiratsuka, S. *et al.* Endothelial focal adhesion kinase mediates cancer cell homing to discrete regions of the lungs via E-selectin up-regulation. *Proc. Natl Acad. Sci. USA* **108,** 3725–3730 (2011).
53. Hiratsuka, S., Watanabe, A., Aburatani, H. & Maru, Y. Tumour-mediated upregulation of chemoattractants and recruitment of myeloid cells predetermines lung metastasis. *Nat. Cell Biol.* **8,** 1369–1375 (2006).
54. Hiratsuka, S. *et al.* The S100A8-serum amyloid A3-TLR4 paracrine cascade establishes a pre-metastatic phase. *Nat. Cell Biol.* **10,** 1349–1355 (2008).
55. Bos, R. *et al.* Biologic correlates of ^{18}fluorodeoxyglucose uptake in human breast cancer measured by positron emission tomography. *J. Clin. Oncol.* **20,** 379–387 (2002).
56. Kang, S. S. *et al.* Clinical significance of glucose transporter 1 (GLUT1) expression in human breast carcinoma. *Jpn J. Cancer Res.* **93,** 1123–1128 (2002).
57. Elmen, J. *et al.* Antagonism of microRNA-122 in mice by systemically administered LNA-antimiR leads to up-regulation of a large set of predicted target mRNAs in the liver. *Nucleic Acids Res.* **36,** 1153–1162 (2008).
58. Elmen, J. *et al.* LNA-mediated microRNA silencing in non-human primates. *Nature* **452,** 896–899 (2008).

METHODS

Cells, plasmids and viruses. Human cancer cell lines and the non-cancerous cell line MCF10A were obtained from the American Type Culture Collection and cultured in the recommended medium. Mouse astrocytes were purchased from Lonza and cultured following the manufacturer's instructions. MCF10DCIS.com (MCFDCIS) cells were purchased from Asterand. The MDA-MB-231-HM cells were generated in our laboratory through explant culture of a spontaneous meningeal metastasis of MDA-MB-231 cells from an immunocompromised mouse, and have been used in our previous study[27]. Mouse lung fibroblasts were isolated from minced lung tissue grown in DMEM supplemented with 10% fetal bovine serum and 10 μg ml^{-1} basic fibroblast growth factor (Life Technologies). The purity of the fibroblasts was confirmed by the expression of FSP-1 in more than 95% of the cells. Neurons were generated from a mouse E14.5 embryo. Briefly, the embryonic brain cortical neurons were differentiated from a primary culture of embryonic neural stem cells by culturing in medium containing N2 supplement (Life Technologies), 0.5% fetal bovine serum, 20 ng ml^{-1} fibroblast growth factor and 20 ng ml^{-1} epidermal growth factor for 5 days on plates coated with Matrigel (BD Biosciences). All cells used herein were tested to be free of mycoplasma contamination. PCR primers 5′-GCACGTCCTCGAGTAGGCCAGCAACGCTTGTAG-3′ and 5′-TTATAATGCGGCCGCAGGTGGAGGGTGGAGTGTTTGCTGC-3′ (for wild-type miR-122 site) or 5′-TTATAATGCGGCCGCAGGTGGAGGGAGATCTGTTTGCTGC-3′ (for mutated miR-122 site) were used to clone the 3′UTR of human *PKM*. Primers 5′-GCACGTCCTCGAGTGGAGACTGGGTGAAAGTGA-3′ and 5′-TTATAATGCGGCCGCACAGCAGGAGTGTATCTTAATCC-3′ (for wild-type miR-122 site) or 5′-TTATAATGCGGCCGCACAGCAGGACAAGATCTTAATCC-3′ (for mutated miR-122 site) were used to clone the 3′UTR of human *CS*. The PCR fragments were digested with XhoI and NotI and then inserted into the same sites of the psiCHECK-2 vector (Promega) downstream of the *Renilla* luciferase gene. For miR-122 overexpression, the hsa-mir-122 gene was cloned by PCR using primers 5′-GCAGCTGAATTCGAGCTGACAAGGTTCCCCTA-3′ and 5′-TAGTACGTCGACAAAGCAAACGATGCCAAGAC-3′, and ligated into the EcoRI/SalI sites of pBABE-Puro or pBABE-GFP retroviral vector. PKM2 and CS overexpressing plasmids were constructed by PCR cloning the full-length ORF of *PKM2* or *CS* using primers 5′-GAAGTTGGATCCAGATCAGGACCTCAGCA-3′ and 5′-GAAGTTGAATTCGGCTCTGGGGTCCATCAC-3′ for PKM2 or 5′-GAAGTTGGATCCTTACCTCCCCACCAGATCC-3′ and 5′-GAAGTTGAATTCACTTTCACCCAGTCTCCA-3′ for CS from MCF10A cells, and inserting the ORF into the BamHI/EcoRI sites of pBABE-Puro. The GLUT1 overexpressing plasmid pcDNA3.2/v5-DEST hGlut1[59] was obtained from Addgene. A lentiviral construct expressing an anti-miR-122 was purchased from GeneCopoeia to generate MDA-MB-231 cells with stable knockdown of miR-122 (MDA-MB-231/122KD). All constructs were verified by sequencing. Target gene knockdown was accomplished using the GeneSolution system, which contains four FlexiTube siRNAs against *Pkm2* (catalogue no GS18746) or *Slc2a1* (catalogue no GS20525, Qiagen). Cell transfection, reporter assays and production of viruses, as well as infection and selection of transduced cells, were carried out as previously described[60]. DRB was purchased from Sigma-Aldrich.

EV purification and characterization. CM was collected from cells grown in medium containing vesicle-depleted fetal bovine serum or horse serum (prepared by overnight ultracentrifugation at 156,000*g* at 4 °C) for 48 h. Dead cells and contaminating cell debris were removed by centrifugation at 500*g* for 15 min and then at 12,500*g* for 20 min at 4 °C. Medium was then subjected to ultracentrifugation at 110,000*g* for 70 min at 4 °C, and the pellet was washed with PBS and subjected to a further round of ultracentrifugation under the same conditions to produce the so-called 110,000*g* pellet that is known to enrich for EVs, including exosomes. The supernatant collected after 110,000*g* spins was concentrated using a Corning Spin-X UF Concentrator with a 30,000 relative molecular mass cutoff (Sigma-Aldrich) and subjected to RNA extraction. When indicated, the 110,000*g* pellet was incubated in 1 μM DiI for 20 min in PBS, followed by a further round of PBS washing. PBS was then used to resuspend the EV-enriched pellets for cell treatment or animal injection. For cell treatment, 2 μg of EVs (equivalent to those collected from about 5×10^6 producer cells) on the basis of protein measurement using the Bradford protein assay (Bio-Rad) were added to 2×10^5 recipient cells. For patient-derived EVs, 1.35 ml of human serum was diluted in PBS to 9.5 ml and filtered through a 0.22 μm pore filter before ultracentrifugation at 110,000*g* for 2 h at 4 °C, followed by a further round of PBS washing. Human sera from BC patients were obtained from voluntarily consenting patients at the City of Hope Medical Center under institutional-review-board-approved protocols. The low-miR-122 serum was from a 62-year-old female patient with ER$^+$PR$^+$HER2$^+$ invasive ductal carcinoma, and the high-miR-122 serum from a 53-year-old female patient with ER$^+$PR$^-$HER2$^+$ invasive ductal carcinoma. Pooled normal serum (catalogue no IPLA-SER) was purchased from Innovative Research.

To further characterize materials in the 110,000*g* pellet for a more precisely defined miR-122 distribution profile, we first adopted a recently established method using AF4 following the previously reported procedure[32]. In brief, the 110,000*g* pellet was resuspended in PBS and injected into an AF2000 system (Postnova Analytics), with an injection loop of 50 μl and a channel thickness of 350 μm. The accumulation wall for the AF4 was a regenerated cellulose ultrafiltration membrane (Postnova), with a molecular mass cutoff of 10 kDa. The flow program for the vesicle separation consisted of a 5 min constant segment with the outlet and cross-flows of 0.3 and 3 ml min^{-1}, respectively, followed by a 15 min ramp-down of the cross-flow to zero flow. Using PBS as running buffer, the eluate exiting AF4 passed through an SPD-20A absorbance detector detecting at 280 nm (Shimadzu), followed by collections every minute on a fraction collector (Bio-Rad; model 2110). On the basis of the established AF4 profile[32] and our sample distribution (Fig. 1e), we combined eluates collected from 8 to 11 min as the 'protein fraction' and those from 18 to 25 min as the 'vesicle fraction'. Although vesicles and low-density lipoproteins are both eluted from 18 to 25 min, low-density lipoprotein is undetectable in the 110,000*g* medium pellet. Each fraction was then divided into two aliquots; one was subjected to RNA extraction using TRIZOL LS reagent (Life Technologies) followed by miRNA assessment by RT-qPCR (see the corresponding section later), and the other was analysed by electron microscopy to verify the absence (in 'protein fraction') or presence (in 'vesicle fraction') of vesicles and characterize their size. For electron microscopy, samples were fixed with 2% paraformaldehyde, loaded on 200-mesh Formvar-coated grids, and then contrasted and embedded as described in ref. 61. The grids were observed under an FEI Tecnai12 transmission electron microscope equipped with a CCD (charge-coupled device) camera.

We also adopted another method to fractionate the 110,000*g* pellet using buoyant sucrose gradient centrifugation following a reported protocol[31]. The pellet was resuspended in 100 μl PBS, diluted to 1 ml in 2.5 M sucrose and loaded into the bottom of a sucrose density gradient ranging from 2.0 to 0.25 M (in PBS) with a 1 ml 2.5 M sucrose cushion loaded below the sample. After ultracentrifugation at 100,000*g* for 6 h at 4 °C, each 1 ml gradient fraction was collected and subjected to RNA extraction followed by miRNA assessment and to electron microscopy as described above. Microvesicle measurements were quantified using Image-Pro Premier software (Media Cybernetics).

BrdU incorporation assay. Cells were plated at 5×10^5 per well on a six-well plate in triplicate. BrdU labelling reagent (Life Technologies) was diluted 1:100 in growth medium. Cells were labelled for 1 h at 37 °C before fixation with 1% formaldehyde and stained using anti-BrdU-APC diluted 1:100 (BU20A, catalogue no 17-5071, eBioscience) before assessment by flow cytometry. Data were analysed using FlowJo software.

2-NBDG uptake assay. After 96 h post-EV treatment, recipient cells were labelled with 100 μM 2-NBDG diluted in glucose-free medium and incubated for 40 min at 37 °C. Fluorescence quantification was carried out using a SpectraMax M3 (Molecular Devices) fluorometer at emission 465/excitation 540 nm. Values were normalized to protein content.

RNA extraction and RT real-time qPCR. These procedures were carried out as described previously[62,63]. Primers used in RT-qPCR are indicated in Supplementary Table 1. The miR-122, miR-16 (as internal control for vesicular miR-122) and U6 primers (as internal control for intracellular miR-122) were purchased from Qiagen. Determination of PKM isoforms was carried out as described[64]. Products of RT-PCR were digested with NcoI, PstI or both enzymes, plus an uncut control, and separated on an agarose gel with SYBR Safe. The presence of a PstI digestion site indicates the splicing isoform M2, whereas the NcoI site indicates isoform M1.

Western blot analysis and PKM activity assay. PKM2 antibody diluted 1:500 (C-11, catalogue no sc-365684) was purchased from Santa Cruz Biotechnology, CS antibody diluted 1:1,000 (catalogue no 16131-1-AP) from Proteintech Group and GLUT1 antibody diluted 1:1,000 (catalogue no ab652) from Abcam. IDH1 diluted 1:500 (D2H1, catalogue no 8137) and IDH2 diluted 1:1,000 (D7H6Q, catalogue no 12652) antibodies were purchased from Cell Signaling. β-actin antibody diluted 1:4,000 (AC-15, catalogue no A1978) was purchased from Sigma-Aldrich. PKM activity was assessed using a protocol modified from Edwards and Watts[65] by diluting each protein sample in 228 μl Solution A (110 mmol l^{-1} imidazole-HCl, 165 mmol l^{-1} KCl, 5.5 mmol l^{-1} $MgCl_2$, 0.19 mmol l^{-1} NADH, 5.5 mmol l^{-1} ADP, 5.5 mmol l^{-1} DTT, pH 7.4) supplemented with 2.5 units lactate dehydrogenase and 62.5 nmol phosphoenolpyruvate (Sigma-Aldrich). Decreases in absorbance of NADH at 340 nm were followed every minute for 10 min after initiation of the reaction. One unit of PKM activity was defined as the amount that will consume 1 μmol of NADH (molar absorptivity 6.22 cm^2 μmol^{-1}) per minute under the assay conditions.

DOI: 10.1038/ncb3094

Medium metabolite analysis. MCF10A-derived cells seeded at equal number were cultured in growth medium containing 3 g l^{-1} glucose but no pyruvate for 72 h before CM was collected, cleared by centrifugation, and subjected to metabolite measurement using a BioProfile 100 Plus (Nova Biomedical). Medium collected from cell-free plates after 72 h incubation was used as the baseline control to calculate the consumption or production of each metabolite, which was further normalized to the cell number in each plate determined at the time of CM collection. MCFDCIS-derived cells were cultured for 48 h before CM was collected for analysis.

Cell metabolome analysis by NMR spectroscopy. Sample preparation, NMR spectroscopy and data analyses were carried out as described[66]. Hydrophilic metabolites dried from the methanol–water fractions were resuspended in 500 µl 100% D_2O containing 3.2 µM 4,4-dimethyl-4-silapentane-1-sulfonic acid, which serves as an internal chemical shift reference and a concentration standard. One-dimensional NMR spectra were acquired at 25 °C on a Bruker Avance spectrometer equipped with a cryoprobe operating at 600.19 MHz ^{1}H frequency. Presaturation was used to suppress water signal, and the spectra were collected with spectral width of 10 kHz, 32 k data points, 3 s relaxation delay and 1,024 transients. ^{1}H NMR spectra of the samples were processed using the Chenomx NMR Suite Processor (version 7.5, Chenomx), and the metabolites were identified and quantified using the Chenomx NMR Suite Profiler. Standard deviation was calculated from triplicate samples.

Animal models: EV conditioning and xenografts. All animal procedures were approved by the Institutional Animal Care and Use Committee at City of Hope and in compliance with ethical regulations. Female NSG mice six to eight weeks old were used here. Exosome-containing EVs were isolated from MCF10A/vec, MCF10A/miR-122 and MDA-MB-231 by the above procedure (for preparation of the 110,000*g* medium pellet) and resuspended in PBS, followed by centrifugation at 16,000*g* for 10 min at 4 °C. The supernatant was then transferred to a new tube for mouse injection. When indicated, EVs were injected into the tail vein of NSG mice biweekly for 3.5 weeks (~6 µg/injection). For cancer cell chase, 1×10^4 luciferase-labelled MDA-MB-231-HM cells were injected inside the heart after preconditioning with six biweekly EV injections; after the cancer cell injection, EV injections continued biweekly for 3 weeks. Orthotopic mammary xenografts were established in NSG mice by injecting 1×10^5 luciferase-labelled MCFDCIS cells or 2×10^5 luciferase-labelled MDA-MB-231/122KD cells or MDA-MB-231-HM cells combined with Matrigel (BD Biosciences) in a 1:1 ratio into the no 4 mammary fat pad. Weekly BLI was carried out using a Xenogen system (Caliper Life Sciences). Tumour volume (mm^3) was assessed by calliper measurements using the formula (width^2 × length)/2. For the miR-122 intervention study, mice were divided into three groups for treatment with PBS, anti-miR-122 oligonucleotides (sequence 5′-CcAttGTcaCaCtCC; 2′-deoxy-2′-fluoro-RNA in capitals, DNA in lower case) or mismatch control oligonucleotides (5′-CcAttCTcaCaCtGC) with a phosphorothioate backbone synthesized at the City of Hope Core of Synthetic and Biopolymer Chemistry. Starting from day 3 after cancer cell transplantation, oligonucleotides (25 mg kg^{-1}) were injected intraperitoneally daily for 5 days and then twice weekly until the end of the experiment.

For 2-NBDG uptake, 15 mg kg^{-1} of 2-NBDG was injected through the tail vein 45 min before a transcardiac perfusion with 1% paraformaldehyde in PBS was carried out to remove the excess dye. Tissues were embedded in Tissue-Tek O.C.T. Compound (Sakura) to make frozen blocks for sectioning and 2-NBDG analysis by fluorescence microscopy. The 2-NBDG signals were quantified using Image-Pro 6.3/Premier software. ATP levels in the tumour samples were prepared by trichloroacetic acid extraction as previously described[67] and assessed by Enlighten ATP assay (Promega) following the manufacturer's instructions.

Co-immunofluorescence. O.C.T. sections were fixed with 4% paraformaldehyde in PBS, blocked and permeabilized with PBS containing 10% goat serum and 0.05% saponin, before incubation with rabbit anti-mouse GFAP diluted 1:500 (Abcam; catalogue no ab7260) for brain or rabbit anti-mouse FSP-1 diluted 1:100 (Abcam; catalogue no ab27957) for lungs together with mouse anti-human CD63 diluted 1:50 (MEM-259, catalogue no NB100-77913; Novus Biologicals). Primary antibodies were then visualized with goat anti-rabbit Alexa 647 IgG diluted 1:300 (catalogue no A-21244) and goat anti-mouse Alexa 594 IgG diluted 1:300 (catalogue no A-11032, Life Technologies). Images were obtained by fluorescence microscopy then pseudo-coloured and merged using Image-Pro Premier software.

Immunohistochemistry and *in situ* hybridization. IHC was carried out as previously described[68] using a 1:400 antibody dilution for PKM2 (C-11), 1:600 dilution for PKM1 (catalogue no NBP2-14833, Novus Biologicals) and 1:250 dilution for GLUT1 (Abcam; catalogue no ab652). ISH was carried out as described[69] using an LNA microRNA ISH miR-122 optimization kit (catalogue no 90003, Exiqon) followed by incubation of sheep anti-digoxigenin-AP (catalogue no 11093274910, Roche Diagnostics), and developed with NBT:BCIP (catalogue no SK-5400, Vector Laboratories) at 30 °C overnight. Nuclear Fast Red was used to counterstain nuclei (catalogue no H-3403, Vector Laboratories).

Glycogen staining. Glycogen staining was carried out using a periodic acid–Schiff kit (Sigma-Aldrich) following the manufacturer's protocol.

Statistical analyses. All quantitative data are presented as mean ± s.d. For all quantitative data, statistical analyses were carried out using Kruskal–Wallis tests. Values of $P < 0.05$ were considered significant. Sample size was generally chosen on the basis of preliminary data indicating the variance within each group and the differences between groups. For animal studies, sample size was predetermined to enable an 80% power to detect a difference of 50%. All samples/animals that have received the proper procedures with confidence were included for the analyses. Animals were randomized before treatments in Figs 5–7. For animal studies, the investigators were blinded to allocation during outcome assessment. For every figure, statistical tests are justified as appropriate, and the data meet the assumptions of the tests.

Repeatability of experiments. For the experiments in which no quantification is shown, images representative of at least three independent experiments are shown.

59. Takanaga, H. & Frommer, W. B. Facilitative plasma membrane transporters function during ER transit. *FASEB J.* **24,** 2849–2858 (2010).
60. Wang, Y. *et al.* Transforming growth factor-β regulates the sphere-initiating stem cell-like feature in breast cancer through miRNA-181 and ATM. *Oncogene* **30,** 1470–1480 (2011).
61. Thery, C., Amigorena, S., Raposo, G. & Clayton, A. Isolation and characterization of exosomes from cell culture supernatants and biological fluids. *Curr. Protoc. Cell Biol.* (2006).
62. Tsuyada, A. *et al.* CCL2 mediates cross-talk between cancer cells and stromal fibroblasts that regulates breast cancer stem cells. *Cancer Res.* **72,** 2768–2779 (2012).
63. Yu, Y. *et al.* Context-dependent bidirectional regulation of the MutS homolog 2 by transforming growth factor beta contributes to chemoresistance in breast cancer cells. *Mol. Cancer Res.* **8,** 1633–1642 (2010).
64. Clower, C. V. *et al.* The alternative splicing repressors hnRNP A1/A2 and PTB influence pyruvate kinase isoform expression and cell metabolism. *Proc. Natl Acad. Sci. USA* **107,** 1894–1899 (2010).
65. Edwards, R. J. & Watts, D. C. Specific spectrophotometric assay for the M isoenzymes of pyruvate kinase in plasma samples containing mixtures of the muscle (M) and liver (L) isoenzymes. *Clin. Chem.* **27,** 906–909 (1981).
66. Cano, K. E., Li, Y. J. & Chen, Y. NMR metabolomic profiling reveals new roles of SUMOylation in DNA damage response. *J. Proteome Res.* **9,** 5382–5388 (2010).
67. Chida, J., Yamane, K., Takei, T. & Kido, H. An efficient extraction method for quantitation of adenosine triphosphate in mammalian tissues and cells. *Anal. Chim. Acta* **727,** 8–12 (2012).
68. Fong, M. Y. *et al.* Withaferin a synergizes the therapeutic effect of doxorubicin through ROS-mediated autophagy in ovarian cancer. *PLoS ONE* **7,** e42265 (2012).
69. Jorgensen, S., Baker, A., Moller, S. & Nielsen, B. S. Robust one-day *in situ* hybridization protocol for detection of microRNAs in paraffin samples using LNA probes. *Methods* **52,** 375–381 (2010).

DOI: 10.1038/ncb3094

nature cell biology

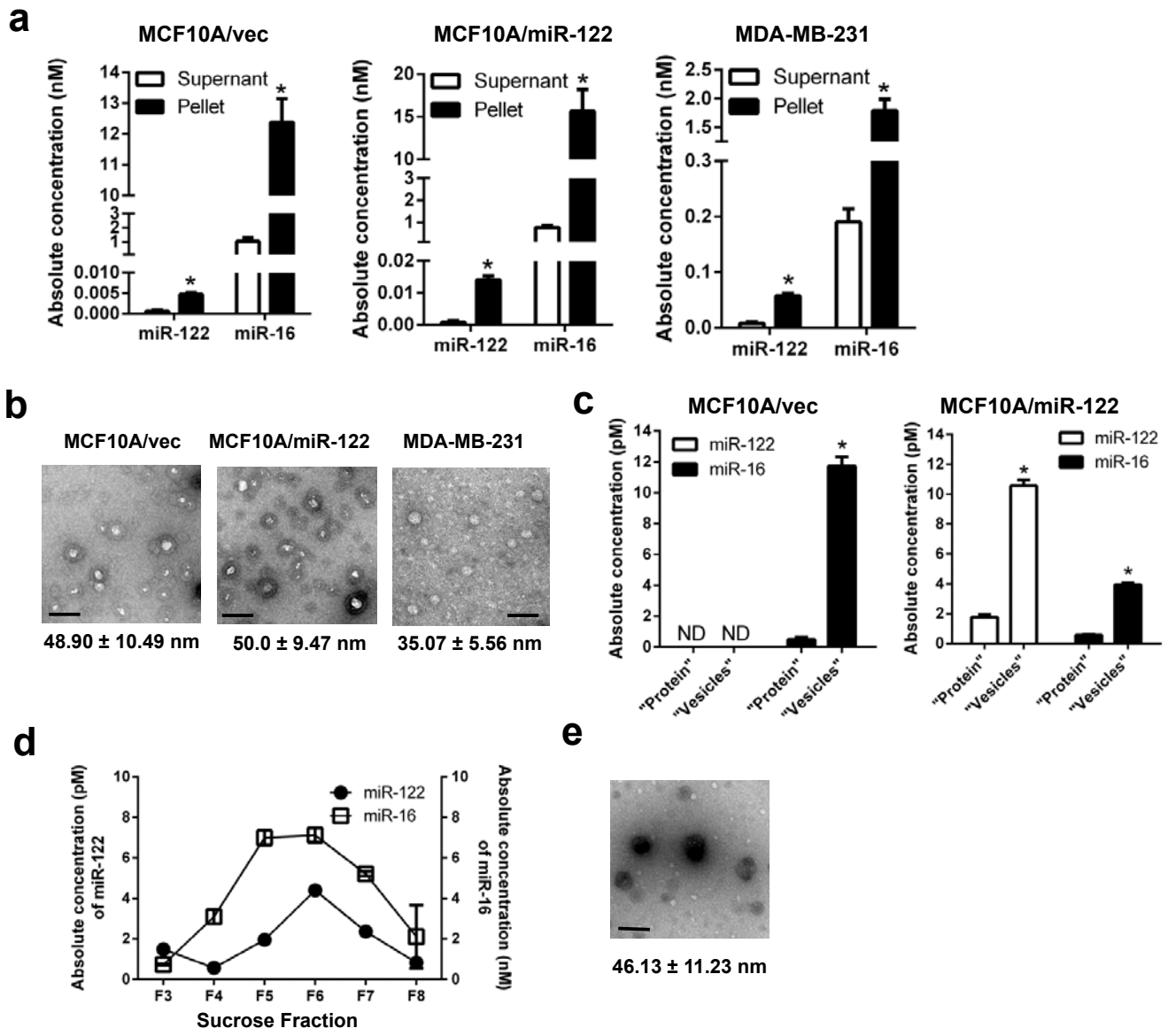

Supplementary Figure 1 Characterization of the 110,000 ×g medium pellet. (**a**) For each cell line, RNA were extracted from the 110,000 ×g medium pellet and concentrated supernatant obtained from equivalent volume of CM and analysed for miR-122 and miR-16 by RT-qPCR. Absolute miRNA levels are calculated based on standard curves (n = 6 extracts). (**b**) Representative EM images of vesicles in the AF4 fraction eluted at 18–25 min. The measured diameter of vesicles was shown as mean ± SD (n = 126 for MCF10A/vec-derived vesicles; n = 222 for MCF10A/miR-122-derived vesicles; n = 41 for MDA-MB-231-derived vesicles). Bars equal 100 nm. (**c**) RT-qPCR-determined levels of miRNAs in MCF10A/vec- and MCF10A/miR-122-derived protein and vesicle fractions separated by AF4. Absolute miRNA levels are shown (n = 6 extracts). ND: not detected. (**d**) Absolute miRNA levels in each gradient fraction after sucrose gradient centrifugation of MCF10A/miR-122-derived 110,000 ×g medium pellet were determined by RT-qPCR (n = 6 extracts). (**e**) A representative EM image of MCF10A/miR-122-derived vesicles in sucrose fraction 6 (F6) (n = 362 vesicles). Bar equals 100 nm. * $p < 0.05$ for all panels derived from Kruskal-Wallis test. Data are represented as mean ± SD in all panels except (**b** & **e**).

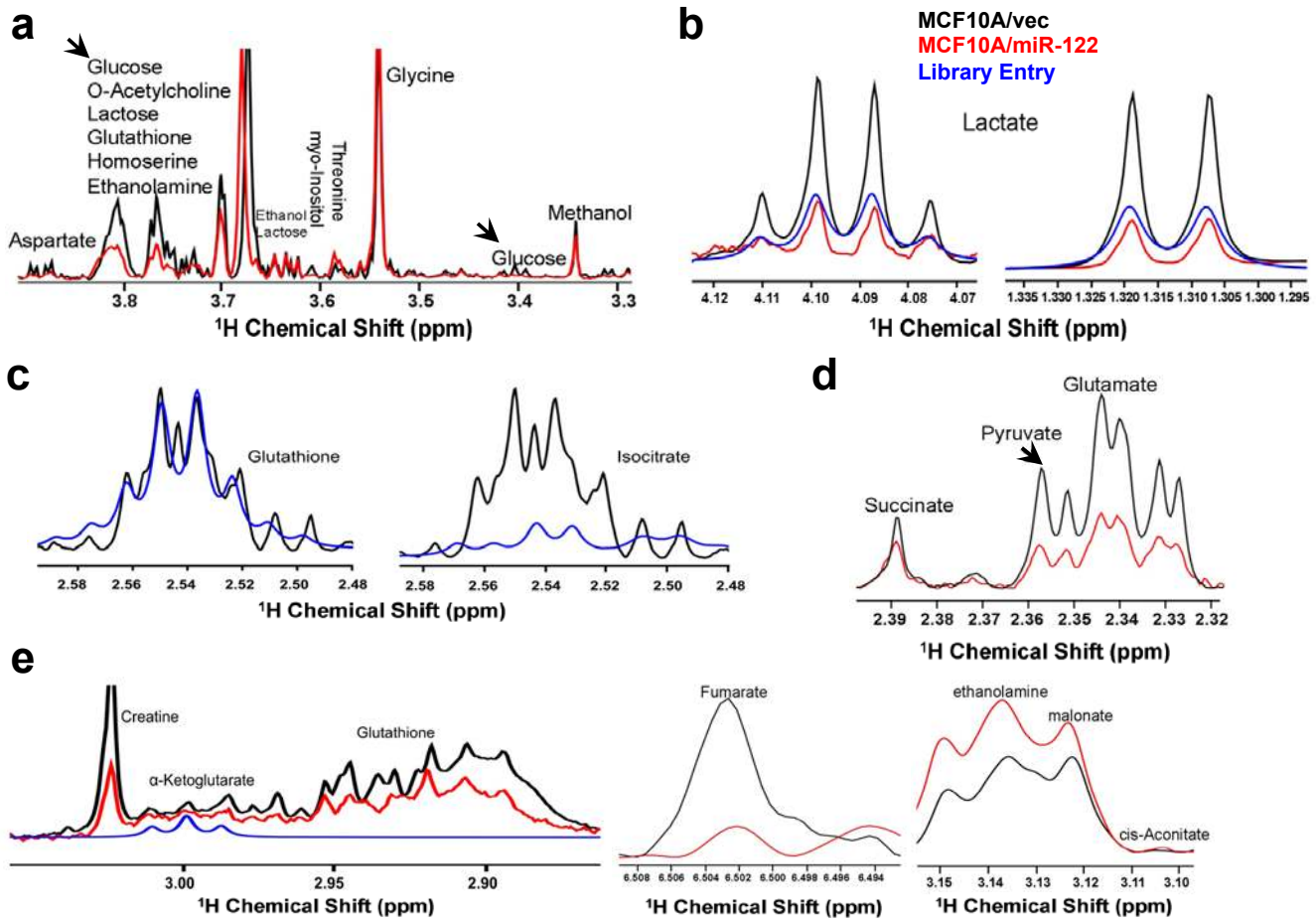

Supplementary Figure 2 Examples of peak assignment based on NMR spectra. For all spectrum snapshots, black represents MCF10A/vec, red represents MCF10A/miR-122, and blue represents library entry. In general, each metabolite produces multiple resonances in different regions of the spectrum. We only analyzed those with some of the resonances that can be resolved unambiguously. An example is given by glucose as shown in (**a**). One of the glucose resonances overlaps with that of O-acetylcholine, lactose, glutathione, homoserine and ethanolamine at around 3.8 ppm, but another glucose resonance is well resolved at around 3.4 ppm. Another example is given by lactate that has peaks in two regions of the spectrum that do not overlap with other resonances (**b**). The unique patterns of NMR resonances, due to J-coupling, are used for de-convolution of overlapping resonances. An example is given in (**c**), which shows that one set of peaks of isocitrate overlaps with that of glutathione, but the patterns of the peaks from the two metabolites are different, and at least one peak of the isocitrate resonance can be well resolved for de-convolution to extract the concentrations. Similarly, the pyruvate peak can be well resolved from those of glutamate (**d**). Examples of assignments of some other resolved peaks are given in (**e**).

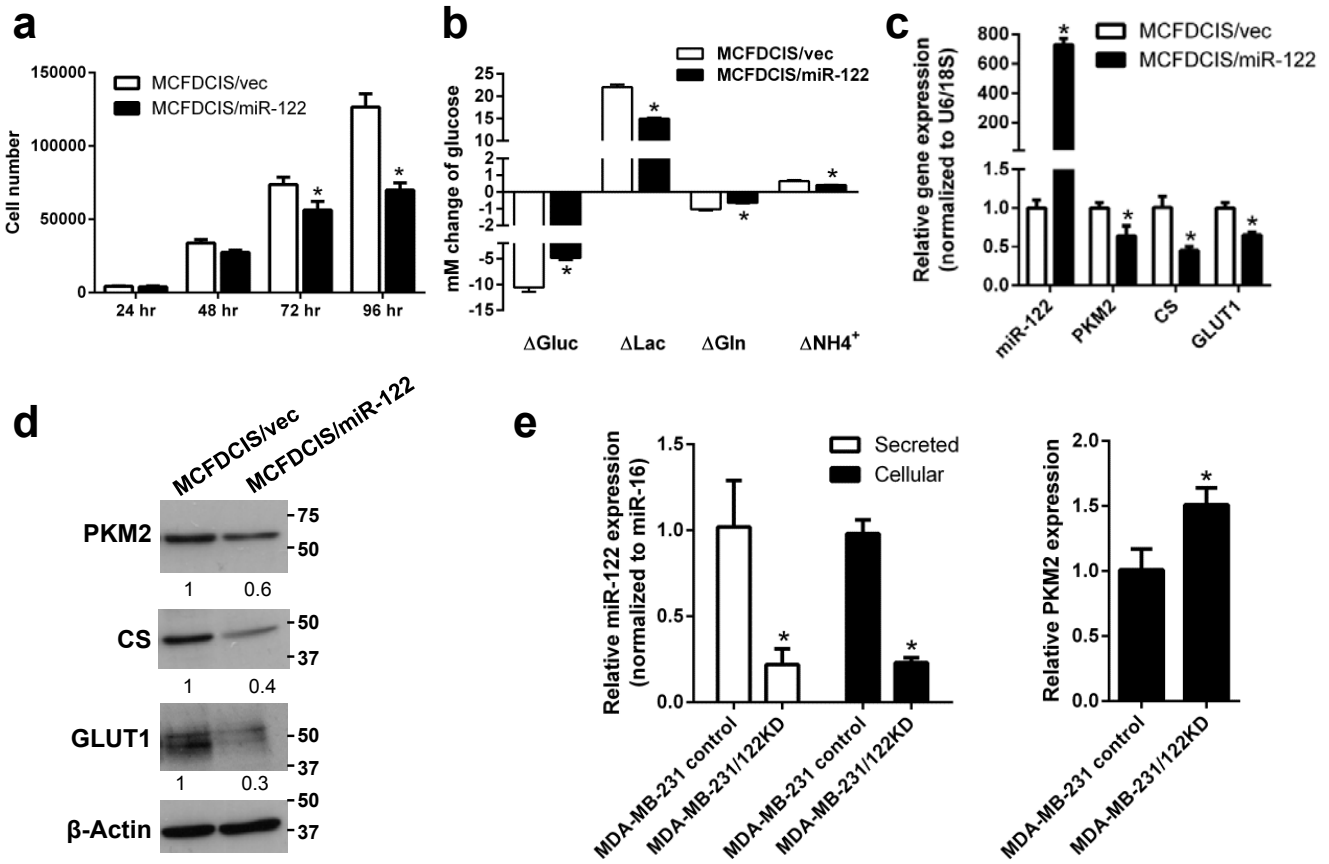

Supplementary Figure 3 Characterization of cell lines with modified miR-122 levels used for *in vivo* studies. (**a**) Cell number counts of MCFDCIS/miR-122 and MCFDCIS/vec cells at indicated time points (n = 6 biological replicates). (**b**) Medium metabolite analysis after 48 h of culture (n = 6 biological replicates). (**c**) RT-qPCR analysis showing the relative expression of indicated genes in MCFDCIS/miR-122 and MCFDCIS/vec cells (n = 6 extracts). (**d**) Western blot analysis in MCFDCIS/miR-122 and MCFDCIS/vec cells. Size of markers (in kDa) are indicated. (**e**) RT-qPCR-determined levels of intracellular and secreted miR-122 as well as PKM expression in MDA-MB-231 cells with stable knockdown of miR-122 (MDA-MB-231/122KD) compared to the control cells (n = 6 extracts). * $p < 0.05$ for all panels derived from Kruskal-Wallis test. Data are represented as mean ± SD in all panels except (**d**). Uncropped, unprocessed images of blots are shown in Supplementary Fig. 5.

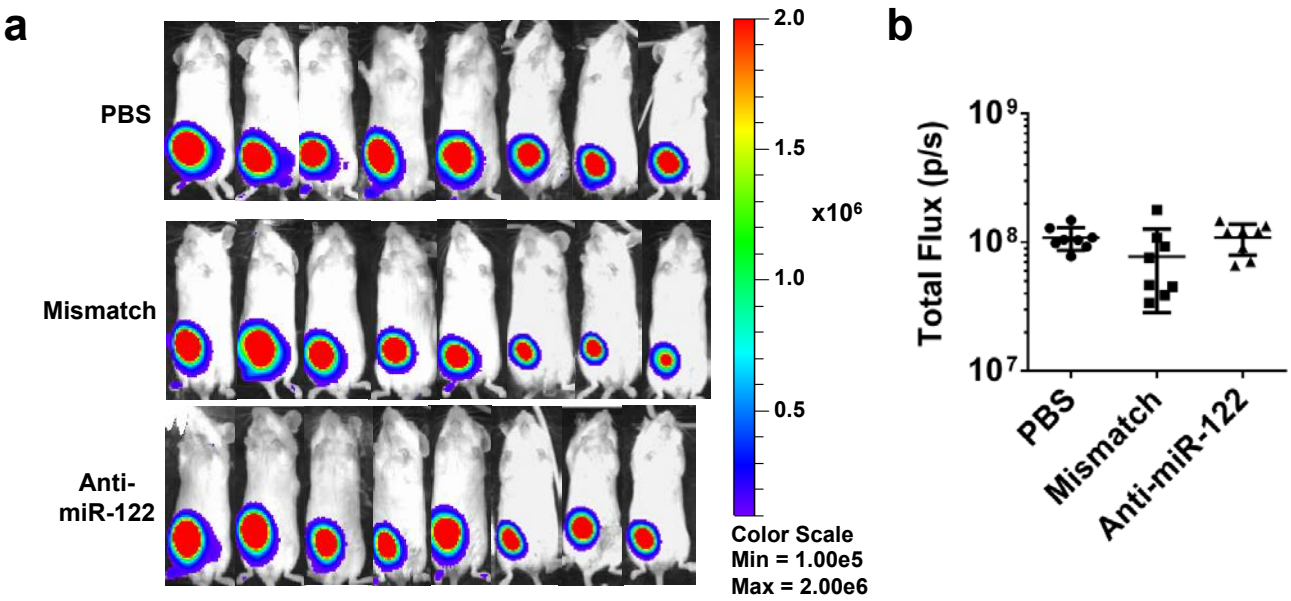

Supplementary Figure 4 BLI of the primary tumours established with MDA-MB-231-HM and treated with anti-miR-122 oligos. (**a**) BLI images at week 3. (**b**) Quantification of (**a**) using Living Image Software (n = 8 mice per group). No significant difference ($p > 0.05$) between groups based on Kruskal-Wallis test.

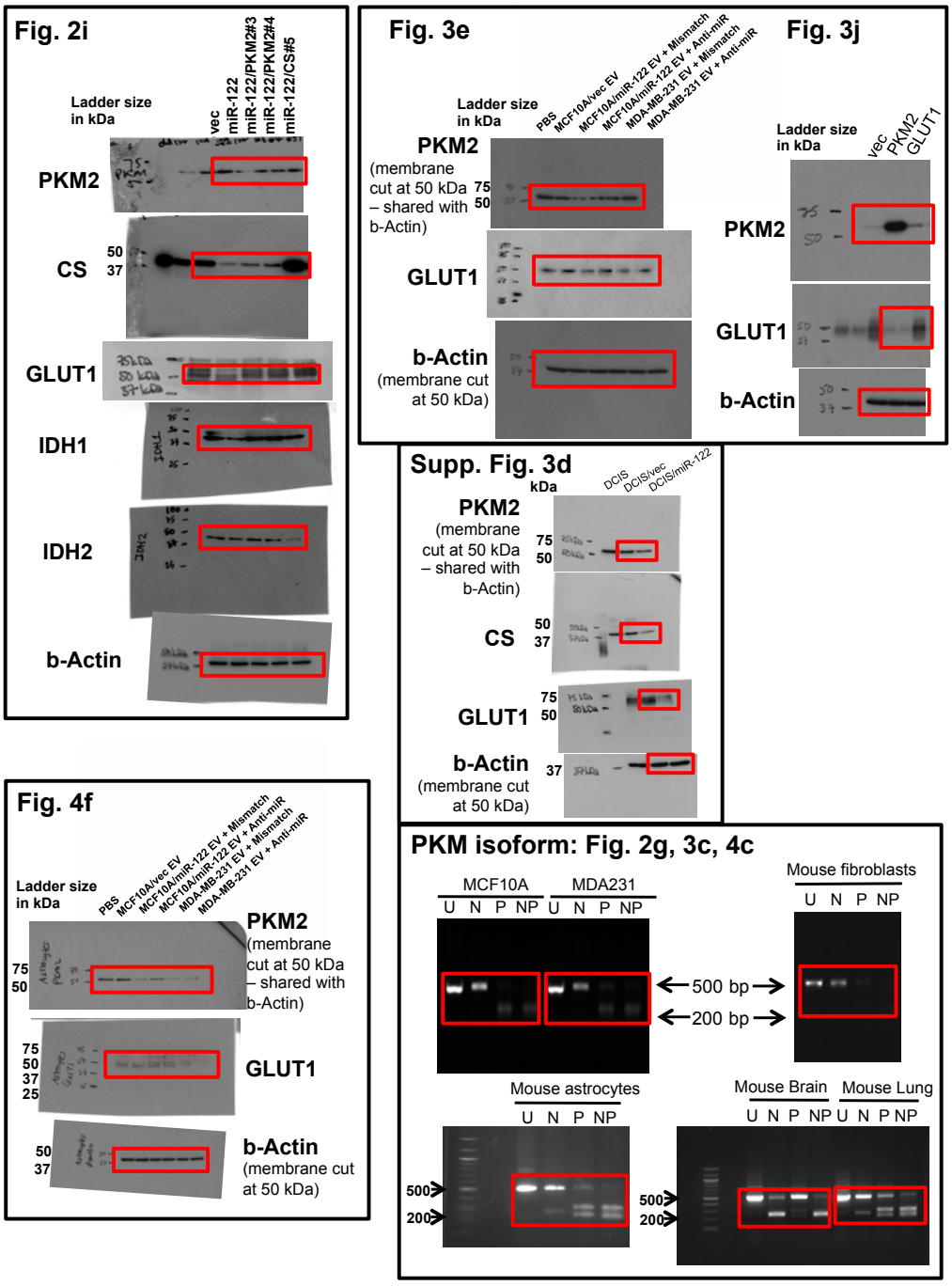

Supplementary Figure 5 Uncropped, unprocessed images of blots and gels.

Gene	Forward primer	Reverse primer	Isoform
Human *PKM*	ATTATTTGAGGAACTCCGCCGCCT	ATTCCGGGTCACAGCAATGATGG	M2
Human *CS*	GGTGGCATGAGAGGCATGAA	TAGCCTTGGGTAGCAGTTTCT	
Human *GLUT1* (*SLC2A1*)	GGCCAAGAGTGTGCTAAAGAA	ACAGCGTTGATGCCAGACAG	
Human *GLUT3* (*SLC2A3*)	GCTGGGCATCGTTGTTGGA	GCACTTTGTAGGATAGCAGGAAG	
Human *GLUT4* (*SLC2A4*)	CTGTCCATCCTGATGACTG	CGTAGCTCATGGCTGGAACT	
Human *GPI*	CCGCGTCTGGTATGTCTCC	CCTGGGTAGTAAAGGTCTTGGA	
Human *HK2*	AACCATGACCAAGTGCAGAA	AGCCCTTTCTCCATCTCCTT	
Human 18S rRNA	CTACCACATCCAAGGAAGGCA	TTTTTCGTCACTACCTCCCCG	
Mouse *Pkm*	GCAGGAACCGAAGTACGC	TGTGTTCCAGGAAGGTGTCA	M1, M2
Mouse *Cs*	AGGCTAGACTGGTCACACAAT	AGGACAGGTAAGGGTCTGAAAG	
Mouse *Glut1* (*Slc2a1*)	GGGCCTAAGGTCACATGAAG	CCAFTFTTATAGCCGAACTG	
Mouse *β-actin*	CGAGGCCCAGAGCAAGAGAG	CGGTTGGCCTTAGGGTTCAG	

Supplementary Table 1 RT-qPCR primer sequences for human and mouse genes.